Energy Calibration of the Münster Dual-Phase Xenon Time Projection Chamber

Kevin Gauda

Masterarbeit

Institut für Kernphysik
AG Weinheimer
WWU Münster

12. Juni 2018

Erster Gutachter: Prof. Dr. C. Weinheimer
Zweiter Gutachter: Prof. Dr. A. Kappes

Eigenständigkeitserklärung

Hiermit versichere ich, dass die vorliegende Arbeit

Energy Calibration of the Münster Dual-Phase Xenon Time Projection Chamber

selbständig verfasst worden ist, dass keine anderen Quellen und Hilfsmittel als die angegebenen benutzt worden sind und dass die Stellen der Arbeit, die anderen Werken – auch elektronischen Medien – dem Wortlaut oder Sinn nach entnommen wurden, auf jeden Fall unter Angabe der Quelle als Entlehnung kenntlich gemacht worden sind.

Münster, den 12.06.2018_____

Ich erkläre mich mit einem Abgleich der Arbeit mit anderen Texten zwecks Auffindung von Übereinstimmungen sowie mit einer zu diesem Zweck vorzunehmenden Speicherung der Arbeit in eine Datenbank einverstanden.

Münster, den 12.06.2018_____

Table of Contents

1 Introduction

Astronomers and cosmologists have gathered a wide range of evidences that large parts of the universe consist of the non-baryonic and non-luminous *dark matter*. Major efforts are being made to reveal its nature, where liquid xenon experiments show the highest sensitivity for the detection of weakly interacting massive particles (WIMPs). Dark matter direct detection experiments based on liquid xenon are constantly developed and growing in magnitude, aiming to be the first to provide evidence of these particles. Coherent WIMP-nucleon elastic scattering in xenon results in scintillation and ionization. The detection of these signals is based on the principle of dual-phase time projection chambers (TPCs), where, at first, direct scintillation light and, at second, charge amplification signals are measured. The dual-phase TPC allows for position reconstruction that is used in dark matter experiments for limiting the detector volume to its inner core, thereby preventing background radiation from the outside to superimpose the WIMP signals. Background events are further reduced by constant purification of the xenon gas. For this purpose, Münster's XENON group contributed a krypton distillation column to the XENON Dark Matter Project to reduce one of the main background sources. The dark matter search within this project lead to the construction of a small-scale TPC in Münster as an R&D device. This thesis approaches the energy calibration of the Münster TPC. The scintillation and ionization of liquid xenon and advantages of liquid xenon detectors with emphasis on dual-phase TPCs are summarized in the second chapter. Chapter three presents the Münster TPC and its stability throughout the measurements, the data acquisition and processing, and the utilized calibration sources. Data quality cuts are introduced in chapter four as well as the reconstruction of the interaction depth. Then, the correction of the acquired data for light and charge collection effects is shown. Chapter five, finally, provides the energy calibration, where both, light and charge signals, are combined for an improved energy resolution.

2 Liquid Xenon Detectors

Liquid xenon (LXe) is used as medium for direct dark matter detection experiments [11], but also for other types of particle detectors. Among them are double beta decay searches [2] and medical imaging detectors [22]. The detector materials' response to energy depositions, the working principle of dual-phase LXe time projection chambers (TPCs) and an energy calibration scheme are outlined in this chapter.

2.1 Liquid Xenon as Detector Medium

Particle interactions in the xenon are measured by the scintillation and ionization signal response of the detector. The generation of these signals is well understood and presented here in short.

Physical Properties of Xenon

As the heaviest stable noble gas[1], with a high atomic number of $Z = 54$ and density of $\sim 3\,\mathrm{g/cm^3}$, xenon provides a high cross-section and stopping power for electromagnetic interacting particles. Basic physical properties of LXe are shown in table 2.1. The xenon phase diagram, shown in figure 2.1, illustrates that xenon is in a liquid state at $-100\,^{\circ}\mathrm{C}$ at 1 atm. Often, LXe detectors are operated under higher pressure than 1 atm to benefit from a wider temperature range of the liquid phase.

[1] Xe-136 is an unstable xenon isotope. It decays via a $2\nu\beta\beta$ process with $T_{1/2} = 2.165 \pm 0.016(stat.) \pm 0.059(syst.) \cdot 10^{21} yr$ [1].

Table 2.1 – Physical properties of xenon.

General Properties	Value
Atomic Number Z	54
Mean Atmoic Weight A	131.30
Density (LXe @ 165.05 K, 1 atm)	3.057 g/cm^3
Tripel Point	161.31 K, 0.805 atm, 1.155 g/cm^3
Boiling Point at 1 atm	165.05 K
Melting Point at 1 atm	161.4 K

Liquid xenon provides a high stopping power for electromagnetically interacting particles like electrons and α particles as well as X-rays and γ-rays [5]. The energy dependent interaction of photons with LXe is described via photoelectric absorption, Compton scattering processes and pair production, where the former process is the most relevant ones for photons with less than 1 MeV energy. The attenuation length is less than 10 cm for 1 MeV photons and decreases with decreasing energy, leading to a high stopping power for lower energies, as figure 2.2 illustrates.

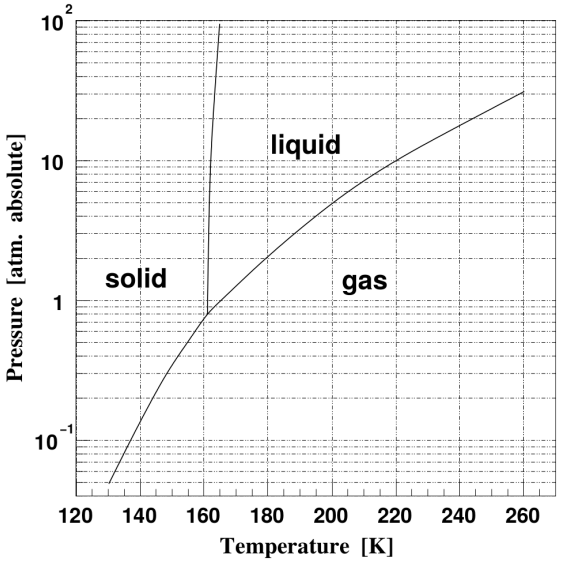

Figure 2.1 – Xenon phase diagram [31].

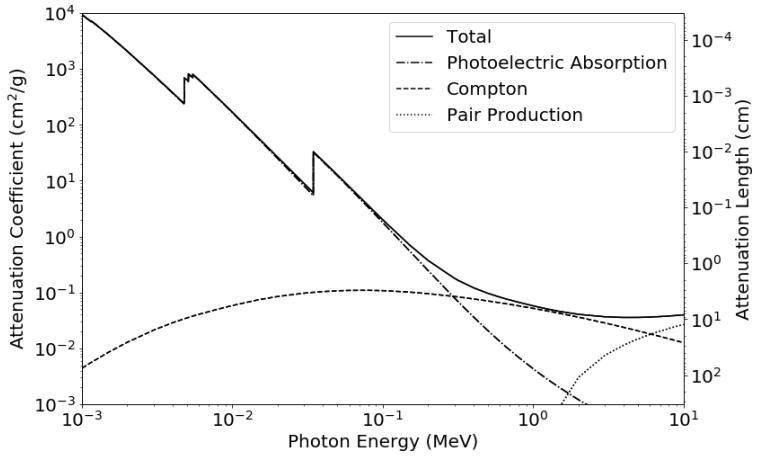

Figure 2.2 – Attenuation coefficient and attenuation length for photons in LXe [15].

Scintillation and Ionization of Liquid Xenon

An energy deposition in LXe induces the excitation and ionization of xenon atoms. Excited xenon atoms (Xe^*) form xenon excimers (Xe_2^*) in the process

$$\begin{aligned} Xe^* + Xe &\rightarrow Xe_2^*, \\ Xe_2^* &\rightarrow 2Xe + h\nu, \end{aligned}$$

[40] resulting in deexcitation and emission of scintillation light of the energy $h\nu = 7\,\mathrm{eV}$, corresponding to a wavelength of 178 nm [23]. Through the process

$$\begin{aligned} Xe + Xe^+ &\rightarrow Xe_2^+, \\ Xe_2^+ + e^- &\rightarrow Xe^{**} + Xe, \\ Xe^{**} &\rightarrow Xe^* + \mathrm{heat}, \\ Xe^* + Xe &\rightarrow Xe_2^*, \\ Xe_2^* &\rightarrow 2Xe + h\nu \end{aligned}$$

xenon ions (Xe^+) contribute to the generation of scintillation light [40]. There is a small fraction of so called escape electrons, that do not recombine.

The application of electric fields results in a reduced scintillation signal from

the latter scintillation process described above, known as scintillation quenching. In exchange for that, there is an increasing fraction of non-recombining electrons with increasing fields. These processes are highly anti-correlated [6], as illustrated in figure 2.3 for 661.7 keV γ-rays.

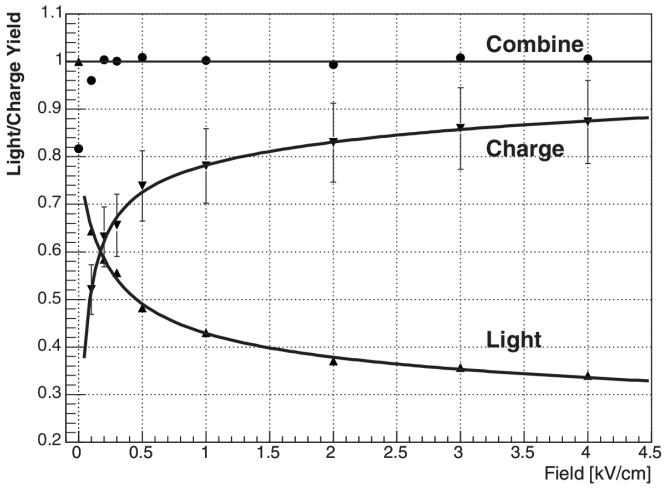

Figure 2.3 – Anti-correlation of scintillation and ionization in LXe for 661.7 keV γ-rays. At increased field strength, the light yield is reduced in favor of an increased charge yield. The combined yield is constant [6].

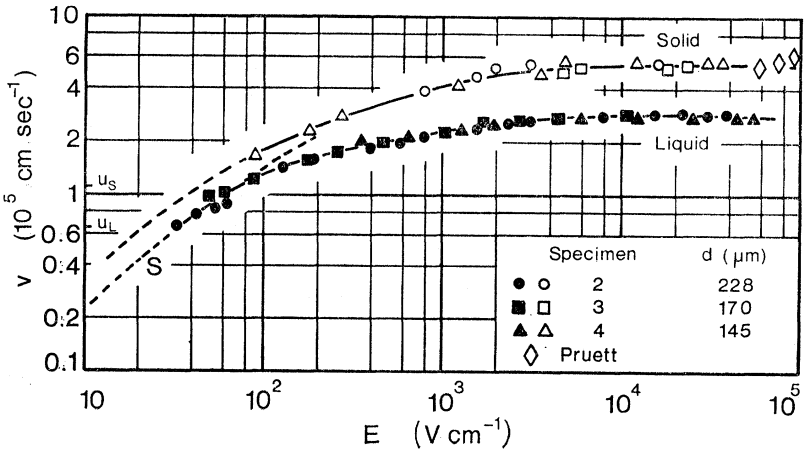

Figure 2.4 – Electron drift velocity in liquid and solid xenon depending on the electric field strength [29].

Electrons in an electric field in LXe are drifted towards the anode. For low fields, the electron velocity is linear dependent on field strength. Increased field strength leads to a non-linear increase of the electron drift velocity v_{e^-}, as shown in figure 2.4.

As electrons drift through LXe in an electric field, they diffuse in transverse and longitudinal direction. While the transverse diffusion broadens the area of the electron cloud that reaches the anode plane and thereby affects the (x, y) resolution of a LXe detector, the longitudinal diffusion causes a smearing in arrival time at the anode that affects the z-position resolution. This spatial longitudinal broadening of the electron cloud is given by

$$\sigma_z = \sqrt{2D_L t}, \tag{2.1.1}$$

where D_L is the diffusion constant for LXe and t is the electron drift time [36].

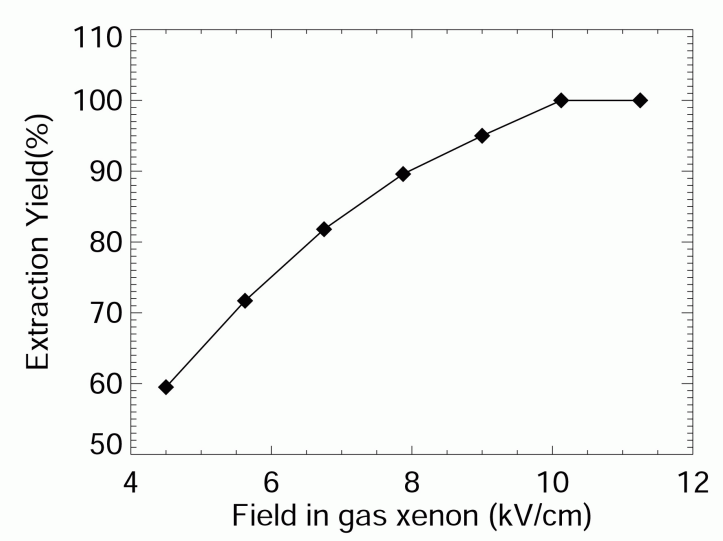

Figure 2.5 – Extraction yield of ionization electrons from the liquid into the gaseous phase depending on field strength [30].

The non-recombining electrons can be accelerated from the LXe surface into the gaseous layer above by an electric field. At high fields, these electrons can gain enough energy to ionize xenon atoms and produce scintillation light. This process is called electroluminescence. The drifted electrons are typically not measured

directly, because the charge amplification measurement benefits from a lower energy threshold compared to direct electron collection. The extraction efficiency depends on the field strength and reaches 100 % for fields larger than $10\,\mathrm{kV/cm}$, as shown in figure 2.5 [30].

Noble Element Simulation Technique (NEST)

Energy deposition in LXe results either in heat, direct scintillation or ionization. Ionization results in scintillation after recombination or in escape electrons. The energy dependence of the scintillation process of LXe is modelled semi-empirically via NEST (Noble Element Simulation Technique) described in [37] and [38]. It combines the Doke/Birks law for long particle tracks and the Thomas-Imel box model for short particle tracks by considering the respective recombination probability after ionization processes. By ignoring heat production from sub-excitation energy depositions, the deposited energy is assumed to be

$$E = W \cdot (n_{\mathrm{ph}} + n_{\mathrm{i}}), \tag{2.1.2}$$

where $W = 13.7eV$ is the effective energy required to excite a xenon atom or produce an electron-ion pair, as used in the model. The effective W value is taken for simplicity, despite the fact that excitation and electron-ion pair generation require slightly different energies W_{ph} and W_{i}, as shown in table 2.2.

Table 2.2 – Properties of LXe regarding scintillation and ionization. W_{ph}, W_{i}, W and F are adopted from [21], [39], [20] and [37].

Ionization Properties	
W_{ph} (LXe)	$(1.8 \pm 0.9)\,\mathrm{eV}$
W_{i} (LXe)	$(15.6 \pm 0.3)\,\mathrm{eV}$
W (LXe)	$13.7\,\mathrm{eV}$
Fano factor F	0.059

The NEST model describes these processes in LXe without electric fields, as well as the scintillation quenching that comes with the introduction of electric fields. Therefore, NEST provides a technique to describe the scintillation and ionization process of LXe detectors from microscopic assumptions and can be used

to estimate the detector's light and charge yield dependent on energy. Equation 2.1.2 gives the basis for the energy calibration over a range of energies, as applied in this work.

2.2 Dual-Phase LXe TPCs

A dual-phase LXe TPC, as operated in Münster, works as detector for energy depositions. The detection principle, the characteristics of this detector type and the path to its energy calibration are shown here.

Working Principle

The detector volume is filled with LXe up to a point between the gate and the anode. Consequently, a xenon gas layer emerges above of that. Liquid noble gas dual-phase TPCs are typically equipped with two PMT arrays, covering the bottom and top area of the TPC. There are different electric fields installed: The drift field E_{drift} ranges from cathode at the bottom of the inner TPC volume up to the gate electrode (grounded). A further electric field between the gate electrode and the anode located above is called extraction field E_{extract}. The LXe container is made from material with a high reflection coefficient for the scintillation light and low intrinsic radioactive background, for example the polymer polytetrafluorethylene (PTFE). A schematic of the working principle of the TPC is shown in figure 2.6, where its capability to distinguish between nuclear and electronic recoils is emphasized.

After an interaction, direct scintillation photons, deexcitation photons from recombination and non-recombining electrons are released. The generated prompt scintillation photons are seen almost instantaneously by the PMTs at the top and the bottom array. This signal is named S1. Electrons that are not recombining with xenon ions are drifted towards the gate electrode by the drift field E_{drift}, where they are strongly accelerated from the liquid into the gaseous volume by the extraction field E_{extract}. This leads to proportional scintillation light, called S2, that is produced via electroluminescence.

Direct dark matter detection experiments on the basis of LXe dual-phase TPCs exploit that dark matter WIMPs are supposed to interact via nuclear recoils,

whereas the dominant background in these experiments comes from electronic recoils. Distinction between nuclear and electronic recoil interactions is possible due to the different scintillation to ionization ratio: in nuclear recoil reactions, a certain energy fraction is lost to e.g. heat or atomic motion, whereas these effects play a minor role in electronic recoils.

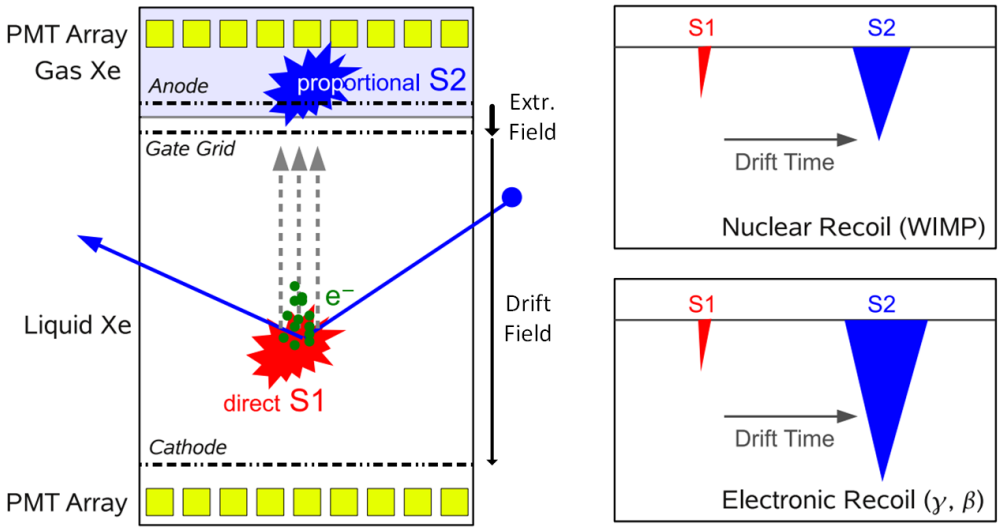

Figure 2.6 – Working principle of a LXe dual-phase TPC, as taken from [8] (modified). The left part shows a particle interaction, causing the prompt scintillation signal S1 and ionization. The ionization electrons are drifted in the drift field towards the gate grid. The charge amplification in the extraction field provides the S2. The event waveforms to the right show the S1s and S2s, where a discrimination between nuclear and electronic recoils is drawn from the S2/S1 ratio.

A great advantage of dual-phase TPCs is that a position reconstruction can be obtained: The z-position can be calculated from the electron drift time t, i.e. the time difference of the S1 to the S2, and the drift length given by the distance from the cathode to the gate electrode. It is linked to the electron drift velocity v_{e^-} via

$$z = v_{e^-} t. \tag{2.2.1}$$

The x- and y-position can be reconstructed by analysing the S2 hit pattern of the top PMTs, where machine learning algorithms and simulations are utilized.

Effects of Impurities in Liquid Xenon

Liquid xenon detectors need to be operated at higher temperatures than other liquid noble gas detectors due to the higher melting point of xenon. As a consequence, some impurities in LXe detectors do not efficiently freeze out, resulting in photon or electron losses [30]. Figure 2.7 shows an overlap of the xenon scintillation spectrum and the absorption spectra of oxygen and water. Small proportions of these substances in the xenon content lead to reduced light collection. The light collection efficiency (LCE) is further, among others, affected by the detector geometry and solid-angle coverage of the PMTs, as well as reflectivity of PMT surfaces, PTFE and xenon.

Drifting electrons suffer losses from absorption by electronegative impurities. Figure 2.8 shows the field dependence of this effect. The number of drifting electrons depends on their drift time t via the absorption law

$$N_{e^-}(t) = N_{e^-}(0) \cdot e^{-t/\tau_{e^-}} \tag{2.2.2}$$

with the number of electrons $N_{e^-}(t)$ and the electron lifetime τ_{e^-}. Thereby, the electron lifetime τ_{e^-} is a quantity to assess the effect of electronegative impurities on S2s.

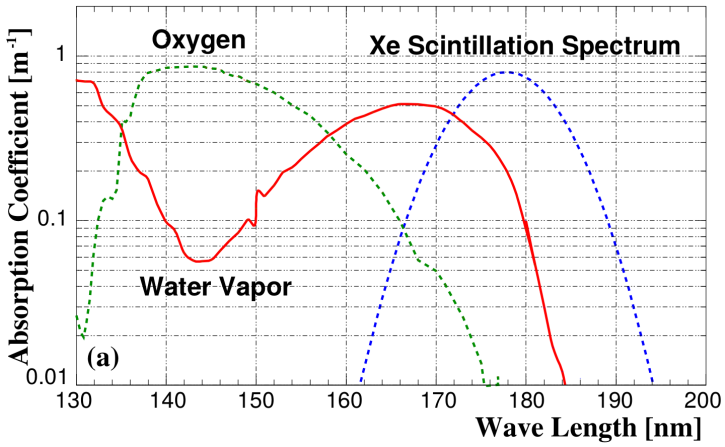

Figure 2.7 – The photon absorption spectrum of O_2 and H_2O and the xenon scintillation spectrum [31].

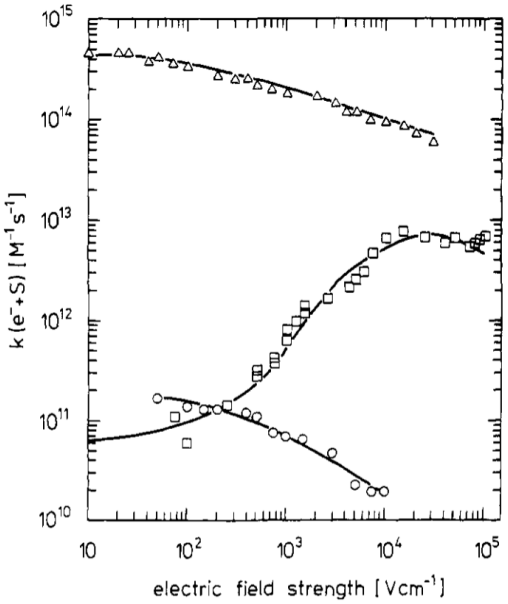

Figure 2.8 – Electron attachment rate k for different electronegative impurities (△: SF_6, □: N_2O, ◯: O_2) in LXe depending on electric field strength [14].

Energy Reconstruction

The advantage of the dual-phase mode of LXe TPCs is the utilization of two readout-channels, i.e. light and charge signals. This results in an improved energy resolution in contrast to the single-phase readout mode [6]. According to the NEST model, the energy of the detector is determined via equation 2.1.2. The number of direct scintillation photons n_γ and drifting electrons n_{e^-}, causing proportional scintillation, are known to be anti-correlated [6]. They are connected with the measured S1s and S2s via the photon detection efficiency g_1 and the charge amplification factor g_2,

$$E = \left(\frac{S1}{g_1} + \frac{S2}{g_2} \right) \cdot W, \tag{2.2.3}$$

where the approach of NEST is adopted to use an effective energy W that is required to excite a xenon atom or produce an electron-ion pair. The proportionality factors g_1 and g_2 depend on the detector properties and need to be determined in order to obtain the energy scale. This is achieved by calculating them from the light yield

$L_y = S1/E$ and charge yield $C_y = S2/E$ of the detector via

$$E = \frac{S1}{L_y} = \frac{S2}{C_y} \tag{2.2.4}$$

and equation 2.1.2. Light and charge yield are the numbers of measured photoelectrons per deposited energy from direct or proportional scintillation. Hence, the charge yield C_y is linear dependent on the light yield L_y:

$$\Rightarrow C_y = \frac{g_2}{W} - L_y \cdot \frac{g_2}{g_1}. \tag{2.2.5}$$

Light and charge yield are determined from calibration sources with known energy.

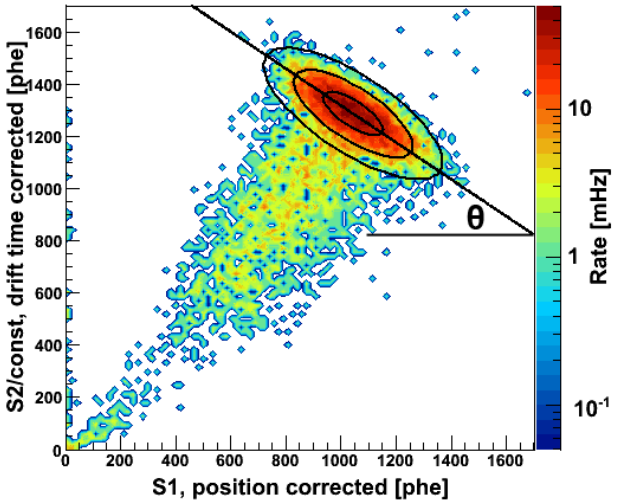

Figure 2.9 – Example for the expression of anti-correlation in the (S1,S2) spectrum [25]. The ellipse that contains the peak is rotated by the anti-correlation angle θ.

In $(S1, S2)$ space, pairs of S1 and S2 with total deposited energy E lie in an ellipse, tilted by the anti-correlation angle θ, as figure 2.9 illustrates for γ-rays from ^{137}Cs in the XENON100 detector. This angle can be utilized to find the combined energy scale with a single energy line. That energy scale is given by the projection of the (S1,S2) distribution along the anti-correlation axis and divided

by a normalization constant ν,

$$E = \frac{S1 \sin\theta + S2 \cos\theta}{\nu \cdot (\sin\theta + \cos\theta)}, \tag{2.2.6}$$

as shown in [6].

The theoretical limit of the energy resolution of noble gas detectors exploiting scintillation and ionization is given by the Fano limit

$$Res_F(E) = 2.35\sqrt{FW/E}, \tag{2.2.7}$$

where F is the Fano factor of xenon that is shown table 2.2. The Fano limit of LXe is comparable to silicon and germanium scintillators [4]. However, fluctuactions of electron-ion yield lead to a lower experimental energy resolution $Res_{\text{exp}}(E)$ [16]. The actual energy resolution follows

$$Res_{\text{exp}}(E) = \sqrt{\frac{A}{E}} + B \tag{2.2.8}$$

with constants A and B depending on these electron-ion yield fluctuations, electronic noise and the Fano limit.

3 The Münster Dual-Phase Xenon TPC

The Münster TPC is a small scale version of the XENON100 TPC. In [34], the original setup and construction is documented. The current setup, the system stability during the measurements for this work, the data acquisition and processing and the calibration sources are described in this chapter.

3.1 Münster TPC Setup

The whole detector system is contained in an insulated stainless steel vessel to keep it isolated from the temperature in the laboratory. A cold head (Leybold COOLPOWER 50) is installed to liquefy the xenon content. The TPC is operated at a pressure of 2 bar, where the temperature range for the liquid phase is increased to almost 20 °C in contrast to 3.6 °C at 1 bar, as the phase diagram in figure 2.1 illustrates, and thereby allows for an easier handle.

The TPC volume is designed for approximately 2.6 kg xenon content and offers an electron drift length of 17 cm. A PTFE housing was built to contain the xenon and as supporting structure for the electrodes, PMTs and other sensors. PTFE was chosen because of its high reflectivity for 178 nm scintillation light [27], as well as for its low field distortion for electric fields in xenon [34].

PMT arrays at the bottom and top, each with seven PMTs[1] (Hamamatsu R8520-06-AL), detect the scintillation light. The same PMT type was used in the XENON100 direct dark matter detection experiment because of its ability to operate under pressure in liquid xenon environment and due to its low intrinsic background. A recent PMT gain calibration was performed in [35].

[1] PMT 5 is currently turned off due to technical issues.

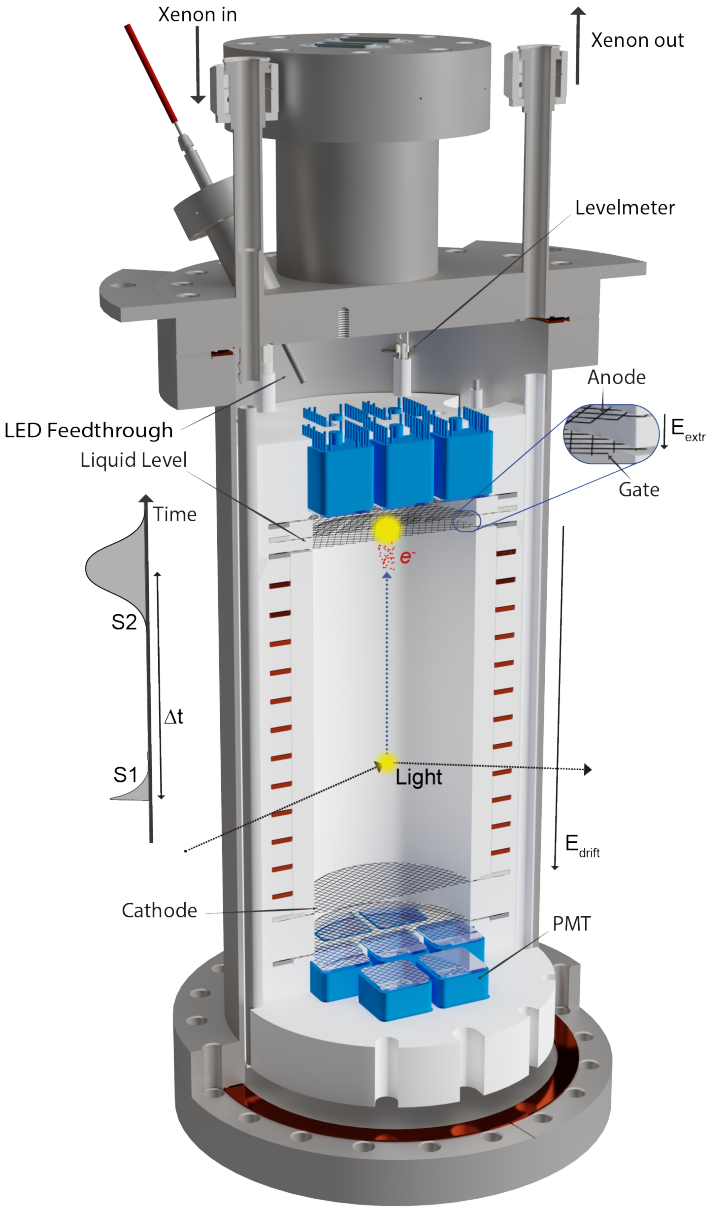

Figure 3.1 – A 3D model of the Münster TPC with the PTFE structure and its sorrounding stainless steel vessel. An evacuated stainless steel vessel insulates the detector system from its environment (not shown). The xenon flow directions into and out of the TPC are marked. The distance between gate and cathode is 168.85 mm at room temperature. The LED feedthrough is used for PMT gain calibration. Drawn by C. Huhmann and modified by H. Schulze Eißing [35].

The voltage for the drift field E_{drift} from the cathode to the gate electrode, supplied by the FUG HCL-35-35000 high voltage module, was set to -8.5 kV, corresponding to a drift field of $E_{\text{drift}} = 0.51\,\text{kV/cm}$. The extraction field was set to $E_{\text{extraction}} = 5\,^{\text{kV}}/_{\text{cm}}$ with an anode voltage of 2.5 kV, supplied via an NHQ 224M high voltage module. The anode is operated below its maximum capability, because there are unresolved problems with higher voltages that are explained further in section 3.2. Additional twelve field shaping electrode rings are installed in the PTFE structure between the cathode and the anode.

A 3D CAD model of the TPC is shown in figure 3.1, emphasizing its working principle as described in 2.2.

Gas System

Before operating the TPC, the detector volume has to be filled with xenon. For this purpose, a gas system is used to transport xenon into or out of the TPC volume. A simplified schematic of the gas system is shown in 3.2. A condenser station, equipped with the cold head (Leybold COOLPOWER 50), is installed to liquefy the xenon gas. From there, the liquid xenon drops into the TPC volume.

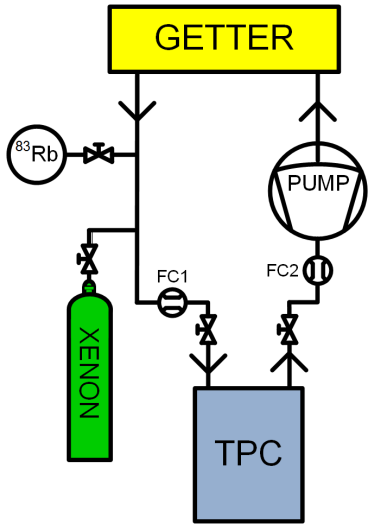

Figure 3.2 – Simpflified scheme of the gas system used during operation and for the filling and recuperation procedure. The ^{83}Rb source provides $^{83\text{m}}$Kr that is used for the energy calibration. The full gas system in more detail is shown in A.1.

The xenon in the TPC has to be cleaned from photon and electron absorbing materials to enable signal generation with a high efficiency. During detector operation, the xenon gas is constantly circulated, driven by the pressure difference exerted by the pump (Chart-Inc QDrive). The gas flow is controlled by the flow controllers FC1 and FC2 (MKS 1579A). The xenon gas passes a hot zirconium getter (SAES MonoTorr PS4-MT15), where electronegative impurities like O_2 or H_2O are taken out of the gas by chemical reactions with the getter material, before being liquefied in the condenser and directed into the TPC. The effect of the purification to the measured data is studied in section 4.5.

3.2 System Stability

As the aim of this work is the energy calibration of the detector and the S2 generation is affected by the liquid level and the electric fields, attention is drawn to the stability of the system. The stability is investigated for the measurement periods of ^{83m}Kr, background and ^{137}Cs that are used as energy calibration sources. Further, some safety-improving updates to the gas system are documented.

Slow Control

Many system parameters – like pressure and temperature inside the TPC – are important criteria, not only for keeping the detector response stable, but also for noticing safety-critical changes in the system. This is why, in case of deviation from specified values, the LabVIEW based slow control is programmed to automatically send out text messages via mail and SMS to the work group. A closer look to the system parameters is provided here for the liquid level and the electric field.

Liquid Level Stability

The pressure and temperature in the TPC directly affect the liquid level. These system properties during the measurements for this work are shown in figures 3.3a and 3.3b. The temperature of the xenon content at the bottom had its mean and standard deviation at $\mu_{\mathrm{TPC,bottom}} = -96.35\,^{\circ}\mathrm{C}$ and $\sigma_{\mathrm{TPC,bottom}} = 0.04\,^{\circ}\mathrm{C}$ throughout the measurements and is considered stable. The pressure $P3$ inside the TPC slightly varied over time. The mean during the ^{83m}Kr, background and

^{137}Cs measurement period variied about less than 1 % from the mean value that is obtained from all measurements combined. However, the stability of the pressure can only indicate the liquid level stability.

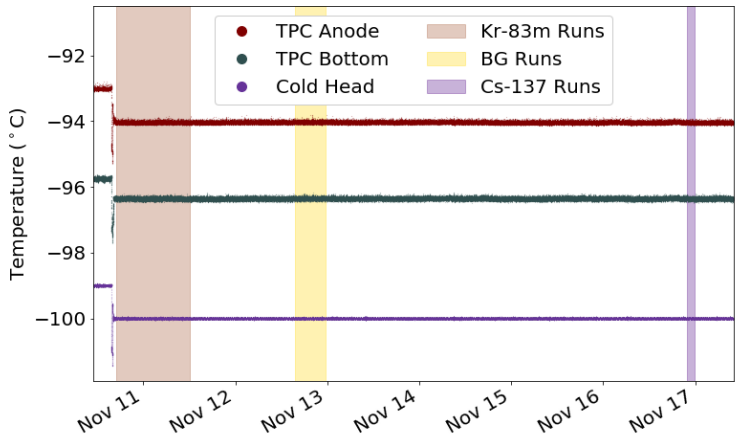

(a) Temperature at bottom and anode position and at the cold head.

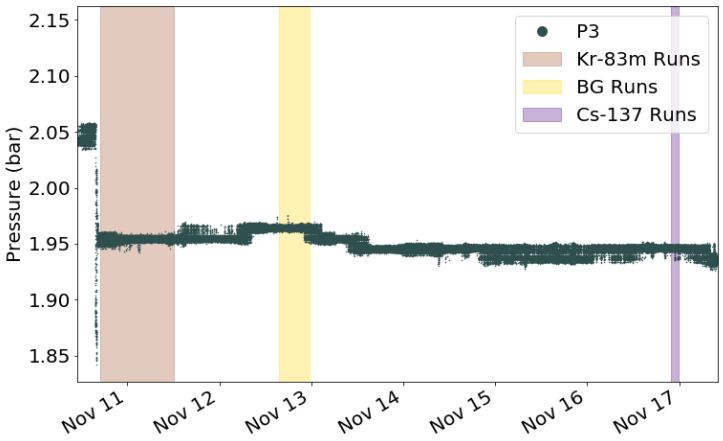

(b) Pressure inside the TPC.

Figure 3.3 – Temperature and pressure in the TPC throughout the measurements used for the energy calibration.

A direct measurement of the liquid level is obtained via capacitive level meters. These are capacitors made from a steel rod inside of a steel tube, as long as the TPC inner volume, to directly measure the change in capacitance when they are filled with LXe. The LCR meter (Agilent U1732C) is precise enough to measure sub-pF changes, where a change in capacity of $0.145\,^{\mathrm{pf}}/_{\mathrm{mm}}$ and sub-mm measurements are expected from [35]. There are three level meters installed, but only one is currently used due to technical reasons. It can be calibrated to the actual liquid level and used to approximately measure the xenon filling height [33], but since the level meters are distorted easily – for example by changing the power supply battery of the LCR-meter, touching the cable and other not yet resolved reasons – they are not reliable for measuring the absolute liquid level over longer time periods. So, an undistorted long-term measurement of liquid level stability, i.e. without drift or sudden jumps and drops, could not be performed with the level meters for the current detector setup, as figure 3.4 shows. The sudden drops originate from a battery change of the LCR meter that is connected to the level meters. There is a drift from the $^{83\mathrm{m}}$Kr to the background measurement period: the mean capacity changed from 219.60 pF to 219.57 pF. The origin of this drift is unknown, but is possibly correlated to the slight increase of the pressure inside the TPC that is shown in figure 3.3b. An influence from outside of the TPC, like the temperature in the laboratory, might be the cause, but an actual change of the liquid level must be considered. A capacity change with filling height of $6.65\,^{\mathrm{mm}}/_{\mathrm{pF}}$ is measured in [35]. Using this value, the liquid level decreased by 0.20 mm between these two measurements, if the drift in capacity originates from an actual level change.

The largest S2/S1 ratio is expected at an optimal liquid level. Therefore, the S2/S1 ratio could be used as alternative to monitor level stability. A calibration source should be used to measure the charge/light yield stability over time at known energy. A study of the S2/S1 ratio at different liquid levels is conducted in [35]. The uncertainty of the liquid level, where the largest S2/S1 ratio is reached, is 0.23 mm, in the same order of magnitude of the liquid level change measured with the level meters throughout the $^{83\mathrm{m}}$Kr and the background measurement. Therefore, small changes of the liquid level throughout the measurements cannot be excluded. Due to the large drop in capacity between the background and the ^{137}Cs measurement, a direct comparison cannot be drawn between the liquid levels.

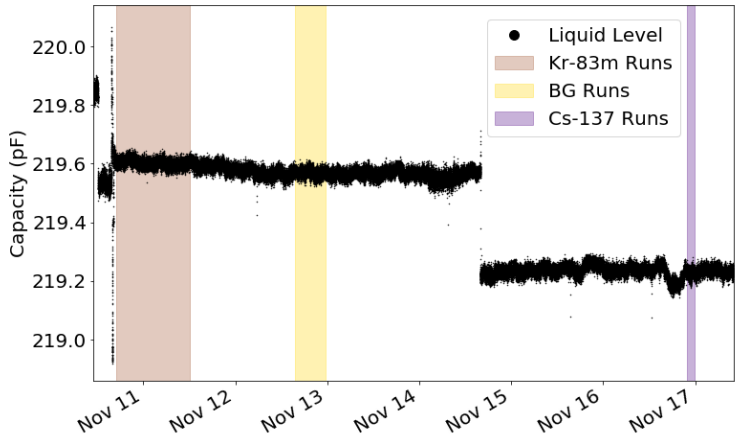

Figure 3.4 – Capacity of the level meters measured with an LCR meter.

Electric Field Stability

The voltage between the cathode and the grounded gate mesh was set to -8.501 kV. No deviations from the destined value were measured within its set precision and so, it is seen as stable to its last digit, i.e. within 0.01 %. With an electron drift length of 166.48 mm, as it is calculated in section 4.3, the drift field becomes $E_{\text{drift}} = 0.51\,^{\text{kV}}/_{\text{cm}}$.

The voltage from the gate electrode to the anode was set to 2.48 kV. With the distance of 5 mm between gate electrode and anode, the extraction field is $E_{\text{extraction}} = 5\,^{\text{kV}}/_{\text{cm}}$. A maximum deviation of 1 % of the mean anode voltage is measured, when only the periods of data taking are compared. It is assumed from figure 2.5, that these instablities have no measurable effect on the electron extraction efficiency and S2 generation. Therefore, the anode voltage is assumed as sufficiently stable during the data taking processes for this work.

Further increasing of the anode voltage lead to an anode drop to 0 kV. The origin of this error was not yet resolved. However, doubling the anode voltage will increase the electron extraction yield to about 100 % compared to the current approximately 60 % to 65 %, as taken from figure 2.5. Resolving the anode instabilities that limit the maximum voltage should be attempted in future studies. No errors occured

during the measurements for the energy calibration and a stable anode voltage could be used in the actual data taking for this work.

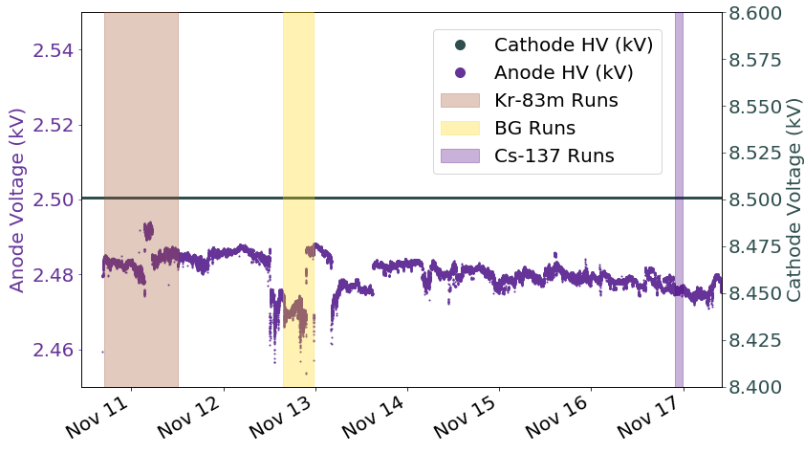

Figure 3.5 – Cathode and anode voltage.

Gas System Upgrades

Keeping liquid xenon under pressure in a cryogenic environment brings the risk of losing valuable xenon or equipment in cases of emergency. To prevent this, a fast recuperation procedure is proven to work in scenarios like power outages. To enhance the security of operating the TPC and the gas system, some updates were acquired as consequence of different incidents.

The gas system contains pneumatic controlled valves that are normally closed and supplied with N_2 gas. At one point of early measurements a leak in the feeding lines for the pneumatic valves with N_2 lead to an uncontrolled escape of N_2, until eventually the valves shut and stopped the gas circulation and forced the pump to be stopped, followed by abortion of the TPC operation and the need for recuperation of the xenon content. A pressure transducer (WIKA A-10) was installed after this incident to monitor the content of the N_2 bottle. In future, it will cause a slow control alarm if the pressure in the N_2 bottle falls below a certain threshold. The QDrive pump temperature is monitored as well to further enhance

the security of the system. An alarm will be sent if the temperature increases over a certain value, indicating a distorted gas flow or cooling water supply problems.

A critical scenario is power failure (total or partial) in the laboratory[2]. The xenon content of the TPC then needs to be recovered and the longevity of sensitive electronic components and the pump system might be affected. Short-term power failures lead to a stop of gas circulation and temperature and pressure increase, but usually, the insulation vacuum isolates the liquid xenon good enough to prevent harsh increases of pressure inside the TPC. Long-term power failures result in an increase of the temperature and pressure up to $\simeq 4\,\mathrm{bar}$ if no action is taken. Then, a rupture disc relieves the TPC content to prevent damage of the PMT's quartz glass and strucure at higher pressures. To safely recuperate the xenon before this happens and constantly monitor the status of the TPC even at power outage, an uninterruptable power supply (APC Smart-UPS X) was installed. The insulating vacuum pressure sensor (CenterOne LED Monitor), sensor microcontrollers (NI cRIO and subsystems), the temperature controller (Lakeshore 336) the slow control PC and the network connection port are therefore accessible for a couple of hours, which ensures a safe recuperation of the xenon content.

A weak point of this system is still, that a failure in the network connection of the slow control PC inhibits alarm messages to reach the recipients. That is possibly dangerous in cases where the network connection and other systems like the temperature controller fail simultaneously. This could be enhanced if an external server monitoring tool would be used additionally to warn in case of network failure. This should be part of future upgrades.

3.3 Data Acquisition and Processing

In this section, the signal chain from the PMTs to the raw data format and the subsequent data processing via the processor for analyzing XENON (PAX) are described.

[2] which indeed happened

Signal Chain

The 14 PMTs translate the VUV scintillation light into measurable electronic signals by amplifying photo electrons (pe) that are emitted from their cathode via photoelectric effect. If one or more PMTs measure a light signal from e.g. a decay in the TPC volume it undergoes the data acquisition (DAQ) process illustrated in figure 3.6.

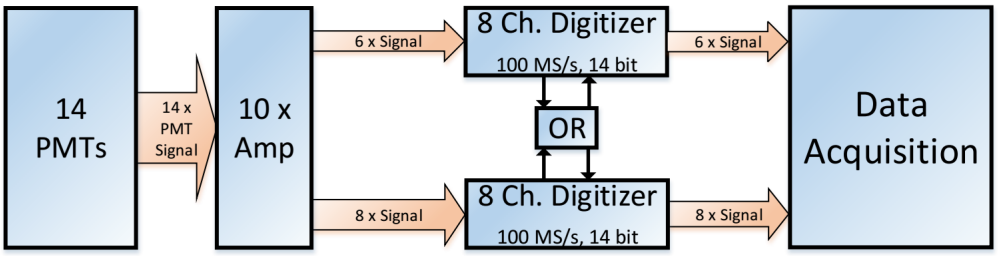

Figure 3.6 – Simplified scheme of the data acquisition process.

At first, the PMT signals are amplified by a factor of 10 (CAEN Mod. N979), then the signals are fed into two identical 8-channel analog-to-digital converter (ADC) units (CAEN V1724). The signals are only sent to the DAQ-PC, if they overcome a certain threshold in both time and amplitude. A trigger signal in one of the digitizer units is forwarded to the other one via a logic 'OR' unit (LeCroy 622 Quad 2-Fold Logic Unit). The signals of both digitizer units are then saved to the DAQ-PC. Everytime the trigger is activated, an event of certain sample size with 10 ns per sample is saved to the DAQ-PC. The current setting is to save 16 k samples or 160 μs in case of triggering.

The trigger used for the datasets analyzed in this work is optimized for S2s. This means that the time and amplitude needed for activation of the data acquisition are too big for S1s. Additionally, the amplitude trigger is set large enough to be not activated by single photo electrons, as a short calculation shows: The PMT gain g, i.e. amplified charge per photoelectron, has been calibrated to approximately $g = 2 \cdot 10^6$ for each PMT. The charge after amplification of a single electron is

$$Q = \frac{U \cdot R}{t} = g \cdot e^{-}, \tag{3.3.1}$$

where the resistance $R = 50\,\Omega$ and sample time $t = 10\,\text{ns}$ are used. The generated voltage of a single photoelectron is then $U = 16\,\text{mV}$ after the 10x amplification. As the input voltage range for the CAEN V1724 14-bit digitizer units is $2.25\,\text{V}_{\text{pp}}$,

$$1\,\text{ADC count} \mathrel{\widehat{=}} \frac{2.25V}{2^{14}} \tag{3.3.2}$$

holds and leads to the amplification of a single photoelectron to roughly 120 ADC counts. An amplitude threshold of 150 ADC counts corresponds to 1.3 photoeelctrons. This amplitude was used as trigger amplitude during most of the measurements in this work[3]. In addition to an exceed of the trigger amplitude, the signal has to endure at least 30 ns to activate the trigger. After a trigger signal, $140\,\mu\text{s}$ in the past – when S1s happen – and $20\,\mu\text{s}$ of the future signal – the tail of the S2 and afterpulses – are recorded. The event is then saved into a raw data file in `.EVE` format by the program `FPPGUI` on the DAQ-PC.

Data Processing with PAX

The PAX processor for analyzing XENON is developed as open source tool for liquid noble gas TPCs by the XENON Dark Matter Project. It is modified to fit the needs of the Münster TPC. The events in the `.EVE` files that are generated in the DAQ process are converted into `.root` files via a step-by-step procedure that is outlined here.

In every PMT channel, PAX looks for amplitudes which overcome a *threshold*. From the first sample to the last sample the amplitude overcomes this threshold, they are counted as **pulses**. If they exceed the *boundary threshold* that lies 5σ above the noise level, they are counted as **hit**. About 70 samples of PMT 13 are shown in figure 3.7. There, several pulses exceed the threshold, but only one is counted as hit as it overcomes the boundary threshold.

[3] In an unsuccessful attempt to reduce the amount of small background signals during the ^{137}Cs data taking, the threshold was set to 1000 ADC counts. That only affects very small signals and does not influence the energy calibration.

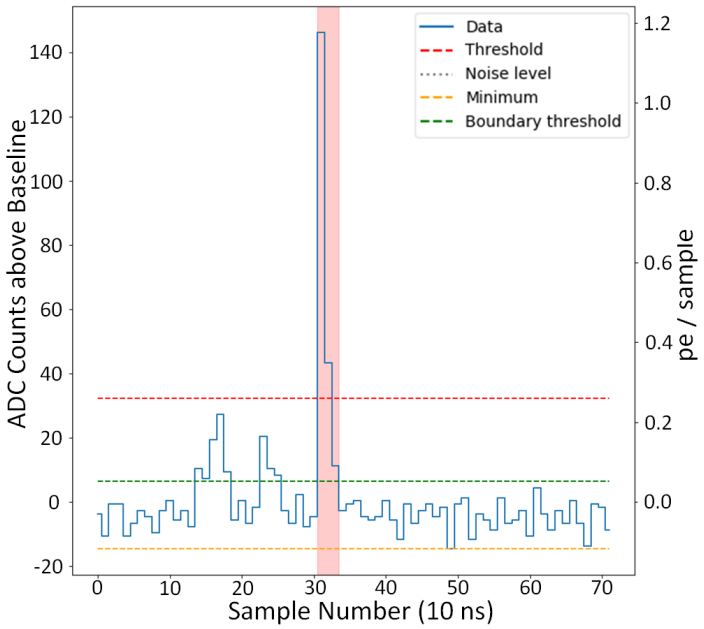

Figure 3.7 – Waveform of a single PMT channel with a highlighted hit. The *threshold* is a 1σ deviation from noise level. Every signal that exceeds the boundary threshold is counted as pulse. A pulse is counted as hit if it exceeds the 5σ *boundary threshold*.

All pulses of the different channels are then summed, if they do not exceed a gap size of a certain sample number. The summed waveform is called **peak** and named *S1* or *S2*, depending on its properties. In the current Münster TPC PAX version 4.9.4 that was used for this work, hits are summed to peaks if there is no 30 ns gap of zero amplitude between them. A peak is currently named S1 if it endures less than 10 samples (100 ns) and S2 if it is broader than 10 samples. S1 and S2 peaks are eventually paired to **interactions** if the S1 causes the S2. PAX needs additional informations that were not yet gathered with the Münster TPC to build these interactions. Therefore, the largest S1 and S2 are used as main interaction throughout this thesis. Finally, all hits, peaks and interactions measured after a trigger form the **event**. An example of an event is shown in figure 3.8, where every peak is classified as S1 or S2. The lower half indicates, which of the PMT channels contributes to the peaks in the upper half.

The processing via PAX results in huge `.root` files not easily accessible to the `python` environment that is chosen for the analysis. So, as a last step, the processed

data is reduced via the Handy Analysis for XENON (HAX) package version 0.3, adapted for the Münster TPC. Only the properties of the event needed for the analysis are thereby transitioned into `python` dataframes. Finally, these dataframes carry the event informations that are used in the analysis.

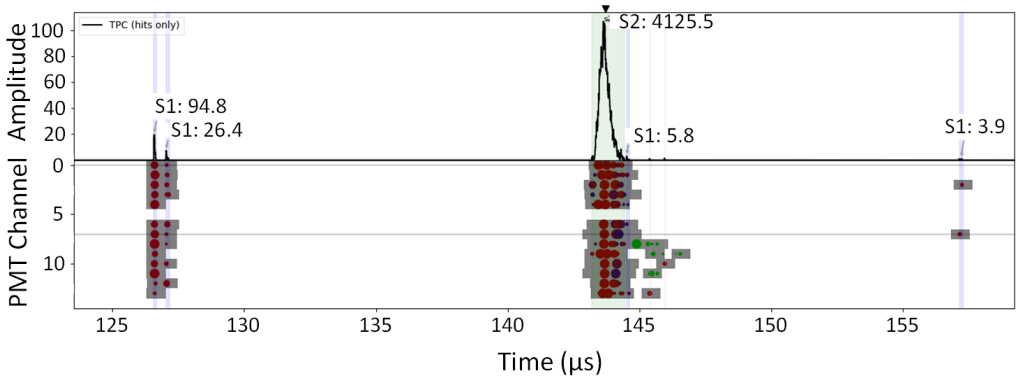

Figure 3.8 – Event waveform of the ^{83m}Kr measurement. The largest two S1s are part of the ^{83m}Kr decay and belong to the S2. The small S1 directly after the S2 is parted from the S2 due to a clustering error. The other small S1 after the S2 is of unknown origin.

3.4 Calibration Sources

The energy calibration of the Münster TPC is obtained with ^{83m}Kr as low-energy source providing energies of 9.4 keV and 32.1 keV and with ^{137}Cs as source of 661.7 keV γ-rays.

^{83m}Kr

With krypton itself being a noble gas, ^{83m}Kr is an isotope that has excellent properties for energy calibration of liquid noble gas detectors. It can be added to the xenon content and is distributed homogeneously in the LXe after an initial mixing time. The decay process of ^{83m}Kr is summarized in a simplified manner in figure 3.9.

^{83}Rb decays via electron capture to one of the excited ^{83}Kr states and remains in an isomeric state at 41.55 keV above the ground state after de-excitation. That is followed by the decay of ^{83m}Kr with a half-life of 1.83 h to the first excited ^{83}Kr state at 9.4 keV above the nuclear ground level. Eventually, the ground state is

reached after a subsequent decay with a half-life of 156.94 ns. The decay energy from ^{83m}Kr to ^{83}Kr is distributed among internal conversion and γ decay.

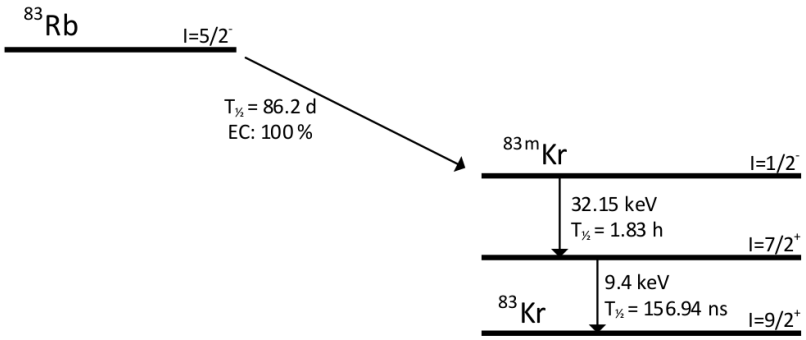

Figure 3.9 – Simplified scheme of the ^{83}Rb decay to ^{83m}Kr and its subsequent decay to the nuclear ground state. With use of [28].

The half-life of 1.83 h from the isomeric to the ground state and the lack of radioactive end products allow it to be safely introduced into the detector without risk of long-term contamination if ^{83}Rb contamination ($T_{1/2} = 86.2\,\mathrm{d}$) is ruled out. An ^{83}Rb source with an activity of $A = 2.6\,\mathrm{kBq}$ (status in November 2017) is directly connected to the gas system.

^{137}Cs

^{137}Cs decays via β-decay to ^{137}Ba with a half-life of $T_{1/2} = (30.08 \pm 0.09)\,\mathrm{y}$. It provides 661.7 keV or 283.5 keV γ-rays, as the decay scheme in figure 3.10 illustrates.

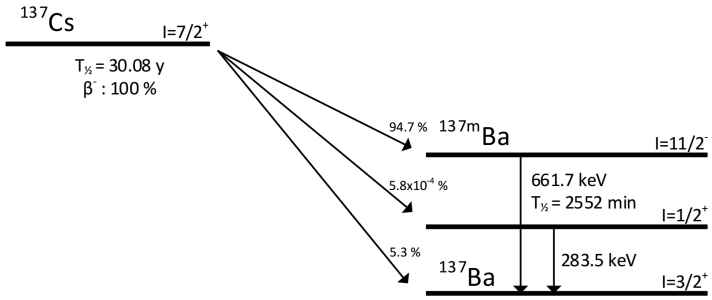

Figure 3.10 – Decay scheme of ^{137}Cs. With use of [17].

A simulated spectrum of the energy deposition of ^{137}Cs γ-rays in the Münster TPC – when placed outside of the detector system – is shown in figure 3.11, where the actual detector response is not modelled [3]. A full-absorption peak at 661.7 keV from γ-rays that deposit their energy in a single interaction inside the liquid xenon is clearly visible. Further simulations in [3] predict that these 661.7 keV γ-rays have enough energy to penetrate the center of the Münster TPC[4] [3]. Scattering processes of the γ-ray, where a proportion of its energy is deposited outside of the detector, lead to the Compton-scattering tail at energies below 661.7 keV. The 283.5 keV γ-rays do not leave a signature in the detector, since their branching ratio is small and they penetrate less deeply into the detector volume due to the shielding by the detector housing and xenon itself. The β-decay electrons are stopped by the housing material of the detector before they can enter the xenon volume.

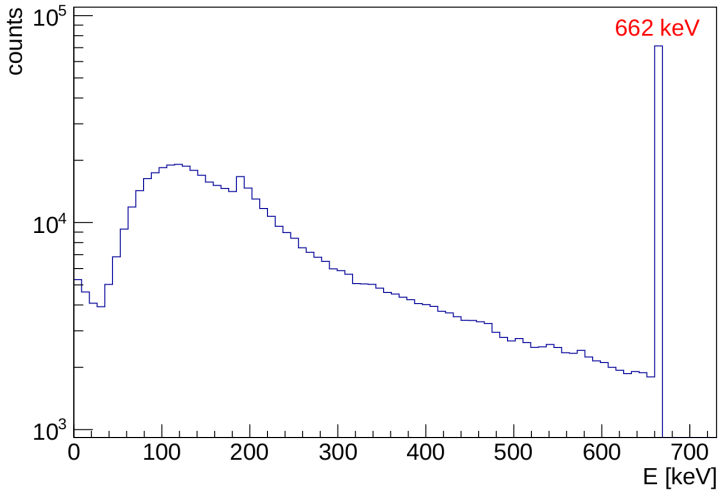

Figure 3.11 – Simulated LXe scintillation spectrum in the Münster TPC from [3] for ^{137}Cs decay γ-rays, where the ^{137}Cs source is placed outside of the vacuum vessel. The detector response is not modelled.

The ^{137}Cs source used for this experiment had an activity of $A = 0.3$ MBq (status in November 2017). It was placed outside of the vacuum vessel at 70 cm

[4] To reach an approximately radially symmetric distribution of signals from ^{137}Cs in the TPC, the source would have to be mounted in at least three equidistant positions outside of the TPC [3]. A calibration of the (x, y)-position reconstruction with ^{137}Cs could then be achieved, which is not part of this work.

height from ground, which roughly corresponds to the height of the liquid volume of the TPC, and about 1 m away of the TPC volume to reduce the event rate. At lower distances the data acquisition system had problems to handle the high rate.

^{57}Co

A 122 keV signature from a ^{57}Co source is typically used as a measure for the efficiency of a scintillator. However, in liquid xenon experiments with large volumes the 122 keV γ-rays cannot penetrate the center of the detector due to the self-shielding [8]. To compensate for that, the detector response can be modelled via the NEST scintillation model, see chapter 2.1, as it is done in [9] and [41]. For the Münster TPC, the detector response at 122 keV is not measured yet, but will be calculated in this work using NEST. Future studies of the detector may try to perform a calibration with ^{57}Co and cross-check the result of this work.

4 Münster TPC Data Analysis

Preparation of the data is key to manage the calibration of the detector. This entails the correct reconstruction of the z-position via the electron drift time, data cuts to reduce unphysical events, and corrections of the light and charge signal.

Since there are effects that change the light and charge signal in dependence of the z-position, one has to correct for them. The light signal correction mainly approaches geometric effects and, therefore, is considered constant throughout the measurements. The charge signal correction aims on electron absorption effects that are expected to be reduced by gas purification over time. A ^{83m}Kr source with properties as described in 3.4 was used to establish the S1 correction. The S2 correction uses both ^{83m}Kr and ^{137}Cs data. The latter were taken five days of continuous purification after the ^{83m}Kr data.

4.1 Data Quality Cuts

Several data quality cuts are introduced here and used on every dataset analyzed within this work to eliminate misleading unphysical signals.

S2-Width Cut

As shown in section 2.1, spatial broadening of the drift electron clouds occurs and eventually leads to signal broadening: The measured S2 shape is a convolution of the diffusively broadened signal with the single electron scintillation signal. The resulting temporal signal width can be expressed as

$$\sigma_t \propto \sqrt{\frac{2D_L t}{v_{e^-}^2} + \sigma_0} \tag{4.1.1}$$

with the electron drift velocity v_{e^-} that is given by the drift field strength, longitudinal diffusion constant D_L and the width of the proportional scintillation signal of a single electron σ_0 [36]. Signals outside a certain range are rejected as unphysical. These are for example noise or random coincidences. A fit with equation 4.1.1 of the mean S2 width depending on the drift time is shown in figure 4.1. Signals within a band of -3σ to $+5\sigma$ signal region are kept. The band is chosen asymmetric due to the asymmetry of the S2 width.

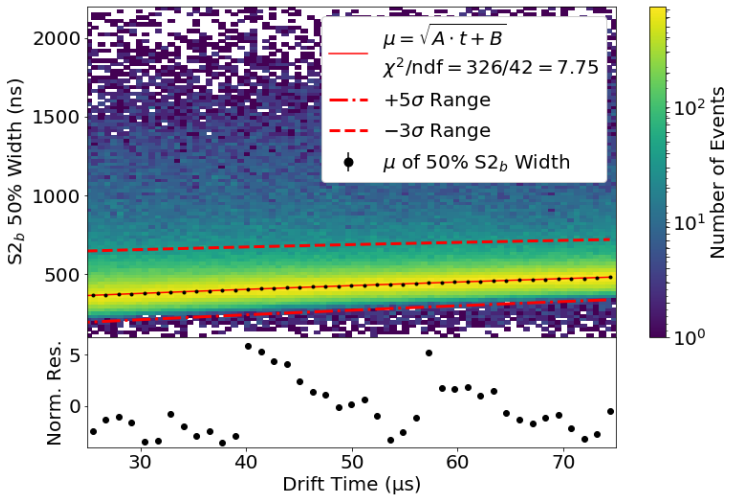

Figure 4.1 – S2$_b$ width depending on the drift time. The mean S2 width μ follows equation 4.1.1. A band of -3σ to $+5\sigma$ around μ is defined that remains after cut application. It is defined asymmetrically to consider the asymmetric S2 width distribution.

S1 Area Fraction Top Cut

The ratio of the S1 area detected by the top PMTs to that detected by the bottom PMTs decreases almost linearly with increasing drift time, as shown in figure 4.2. The decrease with drift time is due to the nearer interaction position to the bottom array. More S1 area fraction is seen by the bottom than by the top PMTs due to total reflection of scintillation light at the xenon liquid-gas interface. To remove random coincidences and noisy events, the area fraction top distribution is divided into drift time slices. A 3σ band around the mean of every drift time slice is kept.

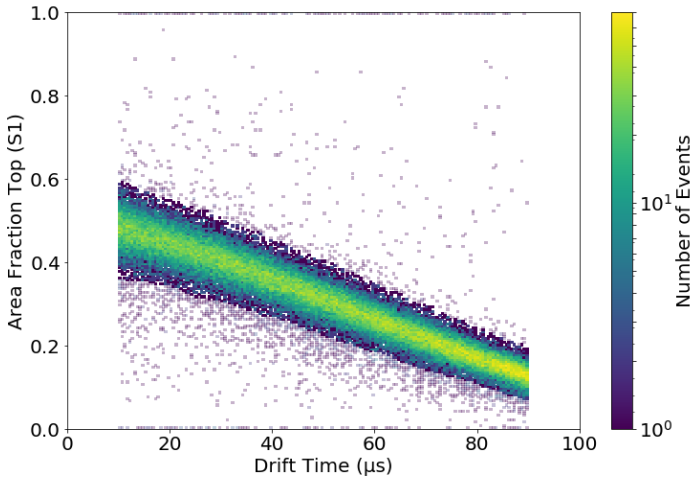

Figure 4.2 – S1 area fraction measured at the top PMTs depending on the drift time.

Sanity Cuts

Events with an S2 measured before an S1 are not causal in the sense that the measured S1s and S2s stem from different interactions and, therefore, are not used further. Events with small largest other S2s below 50 pe are discarded as well, since they most likely correspond to single-electron events. As stated in [10], these single-electron events originate mainly from photoionization of impurities in the liquid xenon and metal components inside the detector volume and are the smallest possible S2.

4.2 ^{83m}Kr and ^{137}Cs Data Preparation

The data used for the depth reconstruction and the S1 correction are coming from ^{83m}Kr due to its easy extractivity, low energy, ideal half-life and homogeneous distribution. In addition to ^{83m}Kr, ^{137}Cs is used for the S2 correction. In addition to the data quality cuts described above, data cuts on the specific event signatures of the sources are applied. These are outlined below.

^{83m}Kr Data Preparation

The trigger rate during the ^{83m}Kr measurement was increased about five percent in contrast to the background measurement. This means, the ^{83m}Kr signal is only a small part of the ^{83m}Kr dataset. However, it can be seperated from background data very efficiently by demanding two subsequently measured S1s within a timespan of ten half-lifes of the ^{83m}Kr state, $T_{1/2} = 156.94\,\text{ns}$. Additionally, a maximum ratio of the first to the second S1 of 15 is set. Thereby, only S1s with a ratio near to $32.1\,\text{keV}/9.4\,\text{keV} \simeq 3.4$ are kept, but variance due to scintillation quenching and the uncertainty principle is allowed. Only the largest S1 and S2 are considered, meaning most of the remaining S1 is assigned to the 32.1 keV signal of the ^{83m}Kr decay. Since no second S2 is demanded, the remaining S2s originate from the 32.1 keV signal or a combined 41.5 kev signal. The signal populations after application of all data cuts are shown in figure 4.3. Only the signals inside the highlighted area remain after S2 width and area cuts for the correction shown in 4.4 and 4.5.

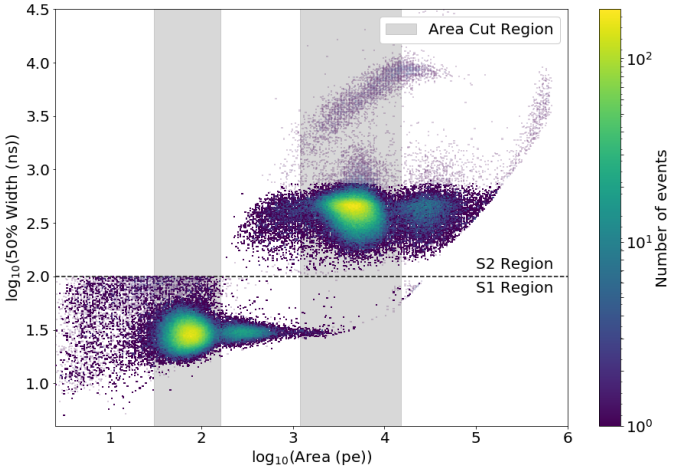

Figure 4.3 – S1 and S2 width depending on the S1 and S2 area of the ^{83m}Kr, where the bleached signals are cut. The S2 width cut reduces large S2s outside of the main S2 region. Background S1s are reduced as well. The highlighted area indicates the S1 and S2 regions that are used for the corrections shown in section 4.4 and 4.5.

^{83m}Kr Decay Studies

Since the increase in rate is very low ($\sim 5\,\%$) after introducing the ^{83m}Kr gas into the system in contrast to the background rate, its presence can be verified from its decay. The half-lifes $T_{1/2}$ of the decay from the 41.5 keV state to the 9.4 keV state and from 9.4 keV to the ground state are investigated. For a measurement of $T_{1/2}$, the decay from 9.4 keV to the ground state, data cuts are used to almost exclusively keep the corresponding signals with 32.1 keV and 9.4 keV, as described in the previous section. An exponential decay fit to the histogram of the time differences of the S1s from the ^{83m}Kr decay, as shown in figure 4.4[1], gives $T_{1/2} = (154.5 \pm 1.9)$ ns in agreement with literature [28].

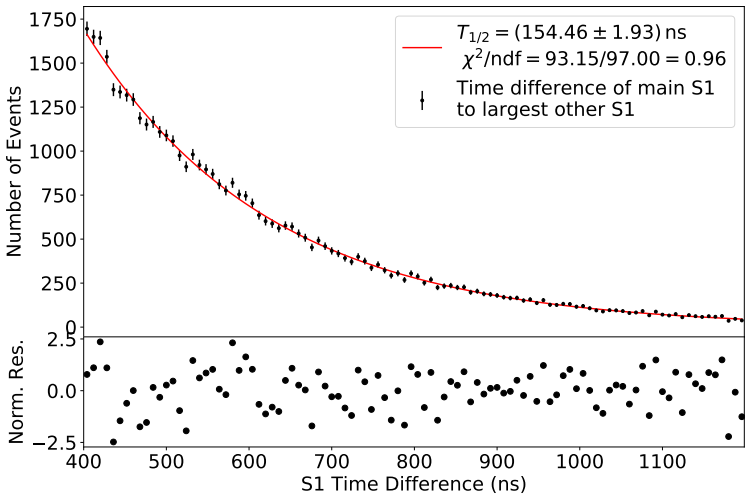

Figure 4.4 – The events in the remaining ^{83m}Kr signal after cuts depending on the time difference between the subsequently measured S1 and $S1_1$ signals, fitted with an exponential decay. The decay time corresponds to the half-life of the 9.4 keV state above the Kr-83 ground level.

The measurement of the 1.83 h half-life of the longer-lived decay between the 41.5 keV and 32.1 keV nuclear energy levels has been demonstrated for a gaseous single-phase operation of the Münster TPC [18]. However, it was not possible to recreate this result in dual-phase mode. Figure 4.5 shows a decrease in the rate

[1] The notation $S1_1$ marks the largest other S1.

of events, each containing a main S1 and a main S2, after the valve to the ^{83}Rb source was closed. No cuts are applied to the data, since they might remove some ^{83m}Kr events and thereby alter the outcome. Instead of the expected $T_{1/2} = 1.83\,\mathrm{h}$, a half-life of $T_{1/2} = (0.94 \pm 0.17)\,\mathrm{h}$ was measured. Since there is a continuous gas flow and liquefaction of xenon and krypton, one has to account for the different vapour pressures of both noble gases. That results in a distillation step in the condenser of the TPC: The relative ^{83m}Kr concentration in the gas is increased with respect to the liquid after every circulation. This can be modelled by investigating the incoming and outgoing number of particles in the TPC volume. The particle change over time can then be described as

$$\frac{\mathrm{d}N(t)}{\mathrm{d}t} = -f_{\mathrm{Xe}}N(t) - \lambda_{Kr}N(t) + \frac{f_{\mathrm{Xe}}}{R}N(t) \tag{4.2.1}$$

$$\Rightarrow N(t) = N_0 \cdot e^{-\lambda_{\mathrm{eff}}\cdot(t-t_0)} \tag{4.2.2}$$

with

$$\lambda_{\mathrm{eff}} = \lambda_{\mathrm{Kr}} + f_{\mathrm{Xe}} \cdot \left(1 - \frac{1}{R}\right). \tag{4.2.3}$$

This is a simplified version of a model shown in [12] that is used to calculate the removal of radon by cryogenic distillation from XENON100. It contains the total number $N(t)$ of ^{83m}Kr atoms in the system, the extraction rate $f_{\mathrm{Xe}} = F_{\mathrm{Xe}}/V_{\mathrm{Xe}}$ with the gas flow F_{Xe} and the circulated xenon volume V_{Xe}, the reduction factor R and the decay constant λ_{Kr} of ^{83m}Kr. Instantaneous homogeneous distribution of krypton in xenon and equilibrium are assumed for simplicity. The first and third term describe the amount of xenon that is circulated over time with a proportion of $f_{\mathrm{Xe}} - f_{\mathrm{Xe}}/R$ flowing back into the TPC after each circulation. Without gas flow and liquefaction, the effective decay constant λ_{eff} would equal λ_{Kr}.

An exponential decay fit is applied to the drop in event rate, that is shown in figure 4.5, to obtain the effective decay constant λ_{eff} from the free parameters amplitude A, constant background C, reduction factor R and effective flow f_{Xe}. A fit constraint is put on the time delay $t_0 = (840 \pm 60)\,\mathrm{s}$, the time after closing the ^{83}Rb valve after starting the measurement. With $\chi^2_r = 1.69$, the model provides a sufficient description of the data. The error profile for the reduction factor R is parabolic to the left, but non-convergent to the right and so, an upper limit cannot

be presented, but a lower limit of $R > 4.9$ at 2σ confidence level can be stated. This is in agreement with the reduction factor $R_{\text{theor}} \simeq 10$ for a single theoretical distillation stage in case of low ^{83m}Kr concentration [32]. Thus, the model 4.2.1 is able to explain the measurements.

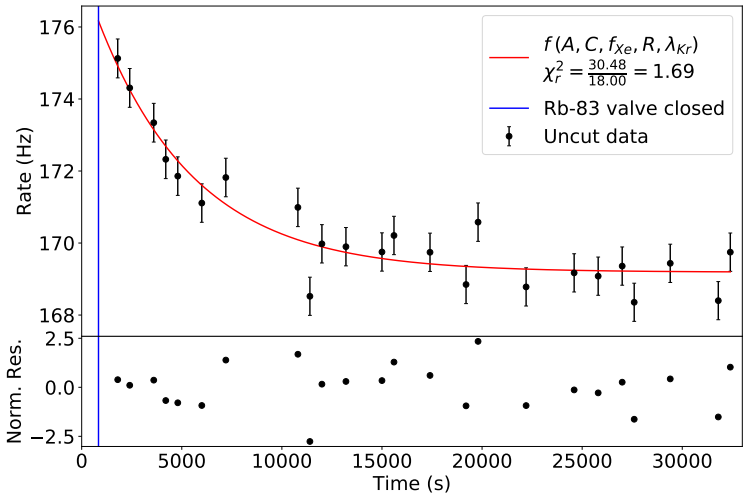

Figure 4.5 – The event rate after closing the ^{83}Rb valve of the gas system. The ^{83m}Kr decay to the 9.4 keV energy level above the ground state and an additional Kr-distillation step need to be considered to explain the exponential fit result.

^{137}Cs Data Preparation

Figure 4.6 shows the (S1,S2) spectrum of the ^{137}Cs dataset, where the full-absorption peak is not clearly distinguishable from the underlying Compton-scattering. If the Compton-scattering happens inside of the TPC, one S1 and two S2s are recorded. Therefore, events coming with more than one S2, where the largest other S2 ($S2_1$) is greater than 10 % of the main S2, are rejected. Events with more than one S1 are rejected, too, because the full-absorption peak is generated by a single interaction and extra S1s cannot originate from the same decay. Only events with a drift time corresponding to $t > 10\,\mu$s and $t < 90\,\mu$s are considered in order to reduce background signals from outside of the detector and from the electronic components in the upper and lower part of the detector. Events originating from the walls cannot be reduced directly due to a lack of (x, y)-position

reconstruction. Instead, the following workaround was used: if the middle PMT of the top array records less than 18 % of the top array S2, the event is assumed to have happenend in the outer region near the walls and is therefore rejected. Eventually, the S2 width cut and S1 area fraction top cut as provided in chapter 4.1 are applied. These cuts will also be used for the energy calibration in section 5.2.

The S2 correction for the ^{137}Cs data in section 4.5 is achieved by extraction of the full-absorption peak via a diagonal cut in the (S1,S2) spectrum. This way, most of the 661.7 keV signals are kept, but signals in the Compton-continuum and background in that region are rejected. The cut is applied along the valley next to the full-absorption peak at an angle that is termed anti-correlation angle. The determination of the anti-correlation angle is presented in detail in section 5.2.

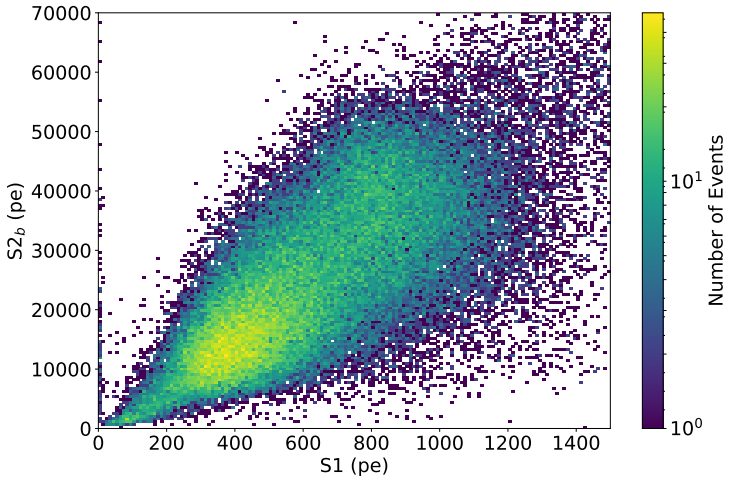

Figure 4.6 – The ^{137}Cs (S1,S2) spectrum after cuts. An additional diagonal cut is applied before the S2 correction in 4.5.

Dead Time Measurement with ^{137}Cs and Background

Despite the S2 correction and energy calibration, the ^{137}Cs data can be utilized to indirectly determine the dead time of the DAQ system by comparing it with background data. The difference by a factor of 2 in the event rates of the datasets is exploited for that purpose. Since DAQ notifications indicate that the measurements

suffer from dead time effects, these are investigated here. No data cuts are applied at all for this study, because they would alter the result of the dead time calculation if they affect the datasets to a different extent.

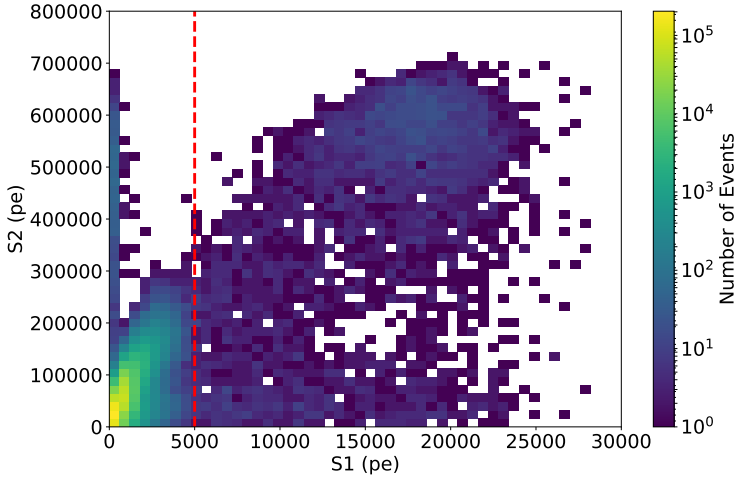

(a) ^{137}Cs spectrum without cuts.

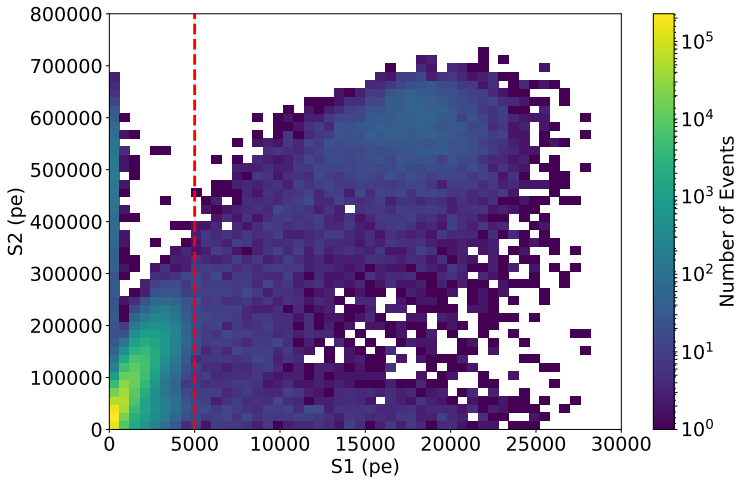

(b) Background spectrum without cuts.

Figure 4.7 – Only S1s greater than 5000 pe are used for the dead time estimation to use exclude any influence of the ^{137}Cs γ-rays.

The dead time is determined from

$$r_{\text{real}} = \frac{r_{\text{meas}}}{1 - r_{\text{meas}} T_d}, \tag{4.2.4}$$

where r_{real} is the unknown real event rate, r_{meas} is the measured event rate, T_d is the dead time and $r_{\text{meas}} T_d$ is the time per second when no data is written [26].

The dead time is caused by a limitation of the DAQ system concerning high event rates: The CAEN V1724 digitizer boards that are mentioned in section 3.3 are equipped with an SRAM buffer that is constantly written in a circular way [19]. If the SRAM is full, no trigger is accepted until one buffer is free and a new event window starts, leading to the detector dead time. An indirect measurement of the dead time induced by this mechanism is presented here. The measured event rate in the ^{137}Cs and in the background dataset are $r_{\text{meas,Cs}} = 336.1\,\text{Hz}$ and $r_{\text{meas,BG}} = 163.3\,\text{Hz}$. A population of signals larger than any possible ^{137}Cs signal that is found in both datasets is used for the measurement of the dead time. These large signals are muonic or radiogenic backgrounds. They are shown in figure 4.7.

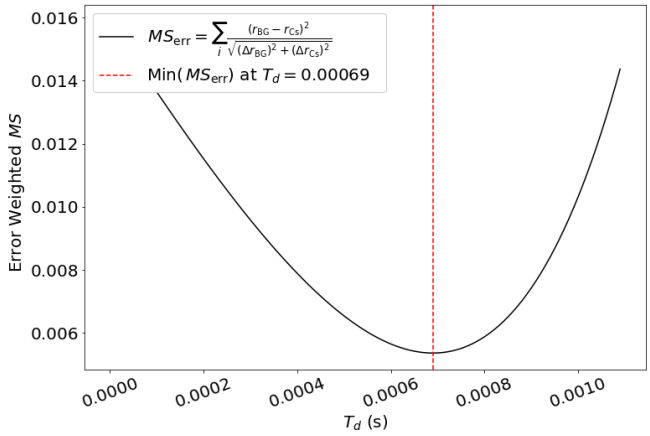

Figure 4.8 – Mean square (MS) deviation of background and ^{137}Cs populations with large S1 and S2. The calculation of the mean square deviation is repeated for different bin widths and left borders.

Since the datasets are measured within five days after another and the xenon content is a hermetic system, the fraction of impurities is assumed to be constant. That allows to compare the size of these populations in both datasets. To exclude

^{137}Cs signals, the left border of the spectra was chosen to be at least 5000 pe. At first, the S1 spectra are normed to the respective measurement duration. Then, the spectra are each divided by $1/(1 - r_{\text{meas}}T_d)$ and subtracted from each other for a range of different T_d. The error-weighted mean square deviation of these differences is calculated, as shown in figure 4.8. The minimum mean square deviation corresponds to the detector dead time. An influence from the bin width and left border of the S1 spectra is observed. Therefore, the procedure is repeated for different left borders from 5000 pe to 10000 pe. The mean and standard deviation from the dead time found with different left borders determine the dead time $T_d = (0.70 \pm 0.02)\,\text{ms}$, where systematic errors are taken into account. So, the real rate of ^{137}Cs and background events are $r_{\text{real,Cs}} = 439.5\,\text{Hz}$ and $r_{\text{real,BG}} = 184.4\,\text{Hz}$. The detector did not record events for $r_{\text{meas,Cs}}T_d = 0.24\,\text{s/s}$ and $r_{\text{meas,BG}}T_d = 0.11\,\text{s/s}$ during the respective measurements.

Saturation Effects in ^{137}Cs

A short investigation showed, that the S2s from ^{137}Cs are affected by saturation. That is not directly visible in the event waveform, but analyses of PMT hits reveal signal clip-offs for S2s in the bottom PMTs, as illustrated in figure 4.9. PMT saturation tends to occur more frequent in signals with smaller drift times, where fewer losses affect the S2. A deeper investigation of saturation effects is needed, but would exceed the scope of this work.

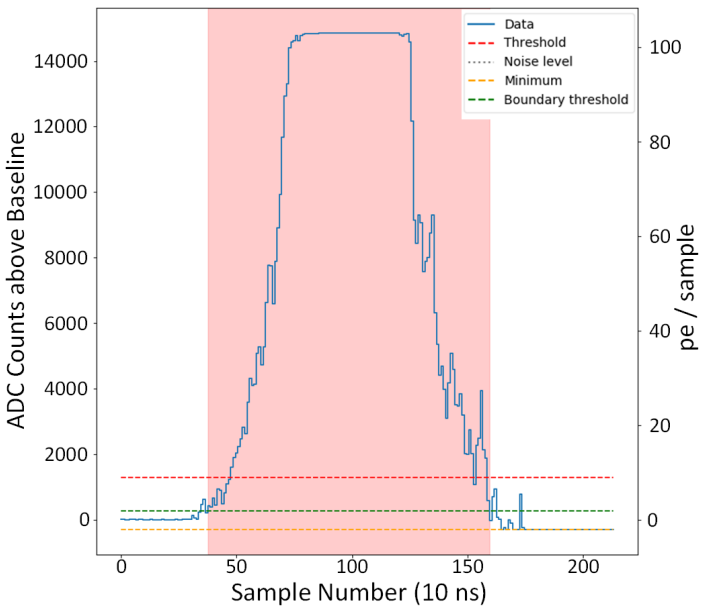

Figure 4.9 – Bottom PMT hit that contributed to the ^{137}Cs full-absorption peak. The clipped-off amplitude is a clear evidence for saturation.

4.3 Depth Reconstruction

Knowledge of the z-position of an interaction is one of the crucial advantages of the liquid noble gas dual-phase TPCs. The homogeneously distributed ^{83m}Kr is used to achieve this for the Münster TPC. The ^{83m}Kr data are prepared as shown in the previous section.

The maximum drift length l_{drift} of the TPC is determined by the distance of the gate to the cathode. The maximum drift length at room temperature is $l_{\text{drift,RT}} = 168.85\,\text{mm}$, as taken from a CAD drawing from C. Huhmann. The linear coefficient of thermal expansion for PTFE from room temperature to the operating temperature of $-100\,^{\circ}\text{C}$ [24] is $\alpha = 112 \cdot 10^{-6}\,\text{K}^{-1}$. The maximum drift length becomes $l_{\text{drift}} = l_{\text{drift,RT}} \cdot (1 - \alpha \cdot \Delta T) = (166.48 \pm 0.36)\,\text{mm}$ after correction of the thermal dilatation. The uncertainty is calculated from the typical 0.1 mm uncertainty for each of the 13 PTFE slices that affects the drift length.[2]

[2]The PTFE structure is a stack of 23 discs, as described in [34]. 13 of them are in the range of the drift field and need to be considered for the uncertainty calculation.

The gate position is set to $z_0 = 0\,\text{mm}$ and the cathode position to $z_{\text{max}} = -166.48\,\text{mm}$. The S2 generation process is reviewed for energy depositions in the small liquid layer between the gate and the anode in order to find the minimum drift time t_0 corresponding to z_0: Due to the strong extraction field $E_{\text{extraction}} \simeq 10 \cdot E_{\text{drift}}$, scintillation quenching leads to a higher S2/S1 fraction in this liquid layer, as it can be seen in figure 4.10a for drift times smaller than $3\,\mu\text{s}$. A constant S2/S1 fraction is measured for drift times greater than $3\,\mu\text{s}$. The S2/S1 fraction, where a 3σ deviation from that is observed, is assumed to correspond to the gate position. This occurs at $t_0 = (1.96 \pm 0.09)\,\mu\text{s}$.

Below the cathode, the electric field does not guide the electron clouds to the gate and therefore, the event count eventually falls to zero. The event count of every imaginary slice z is assumed to be Gaussian distributed due to electron diffusion. The electric field is approximately described by a rectangular function. This leads to a Gaussian smearing of the drift time distribution of events. The maximum drift time is therefore assumed to be half way to the maximum of the drift time distribution at $t_{\text{max}} = (98.78 \pm 0.33)\,\mu\text{s}$, as shown in figure 4.10b.

Eventually, the z-position is calculated via

$$z = \frac{-l_{\text{drift}}}{t_{\text{max}} - t_0} \cdot (t - t_0). \tag{4.3.1}$$

With equation 2.2.1 the electron drift velocity in the detector setup used for this work is calculated to

$$v_{e^-} = (1.72 \pm 0.04)\,{}^{\text{mm}}/_{\mu\text{s}} \tag{4.3.2}$$

at an electric field of $0.51\,{}^{\text{kV}}/_{\text{cm}}$. This result is in agreement with the drift velocity measured in the XENON100 experiment of $v_{e^-} = 1.73\,{}^{\text{mm}}/_{\mu\text{s}}$ at $0.53\,{}^{\text{kV}}/_{\text{cm}}$ drift field [9].

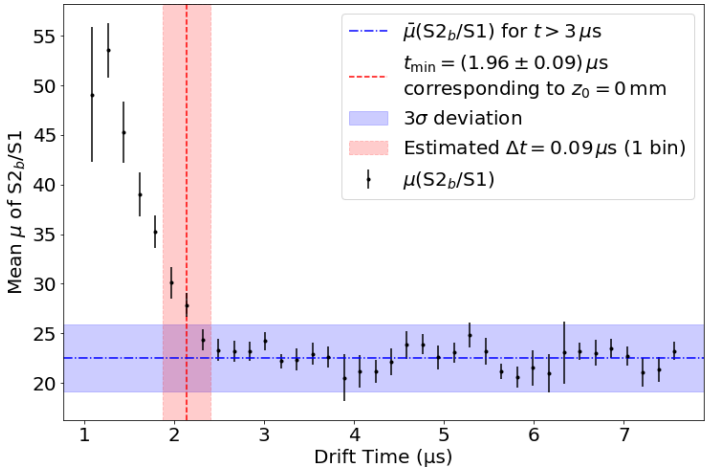

(a) $S2_b/S1$ ratio in dependence of the drift ime. The deviation from the mean $S2_b/S1$ at $t = (1.96 \pm 0.09)\,\mu s$ coresponds to the gate electrode.

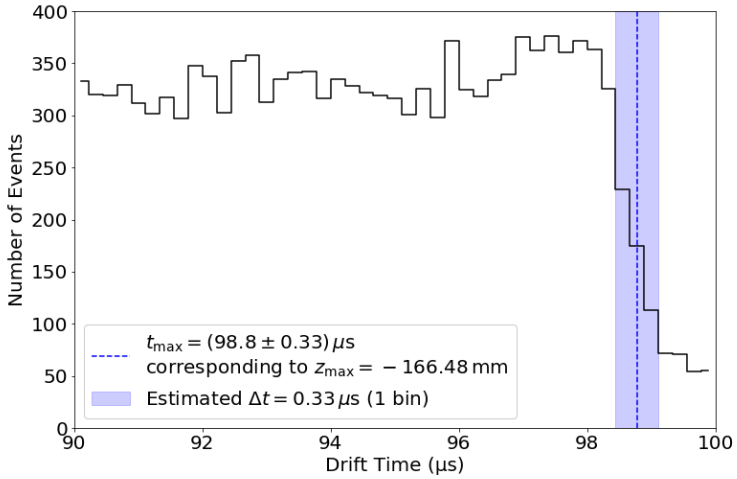

(b) The event count depending on drift time is shown for cut ^{83m}Kr data. The drop in the event number at $t = (98.8 \pm 0.33)\,\mu s$ corresponds to the cathode position.

Figure 4.10 – The z-reconstruction is obtained by finding the drift times corresponding to the cathode and gate position.

4.4 S1-Correction

There are several influences on the total light collection efficiency (LCE) like detector and PMT geometrics, xenon and PTFE reflectivity, and PMT photocathode efficiency. Xenon itself cannot absorb its scintillation photons, but the influence of photon absorption on the LCE increases with increasing amount of impurities. It is assumed due to the constant purification of the Münster TPC that the photon absorption is negligible.

The LCE-correction in this chapter only corrects for geometrical effects in z-direction. LCE-correction of the x, y-dependent effects requires x, y-reconstruction that is not yet implemented for the Münster TPC.

The first step of the LCE correction is to seperate the (z, S1) spectrum into z-slices. The mean S1 is obtained by a Gaussian fit for every z-slice. A search for the mean S1 is obtained in `python` via the `migrad` function from the `iminuit` package to minimize the χ^2 of the fit. This is done iteratively for every z-slice. The bins in z-direction are set wide to reduce the effects of statistical outliers in the S1 distribution. Each z-slice therefore contains an S1 distribution that is averaged over one z-bin. This enlarges the reduced chisquare value χ^2_r, but the fit routine reliably finds the mean S1 of every z-slice, as shown in the example in figure 4.11.

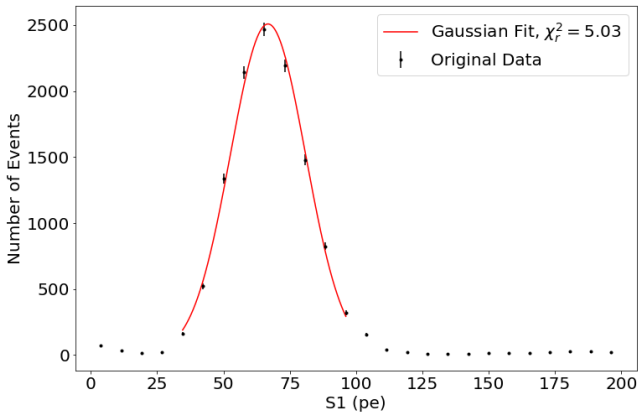

Figure 4.11 – S1 distribution for one of the z-slices, fitted with a Gaussian function.

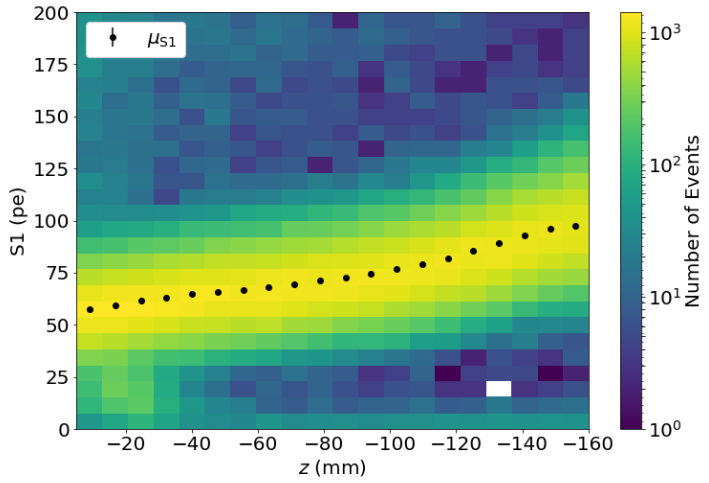

(a) Before LCE-correction.

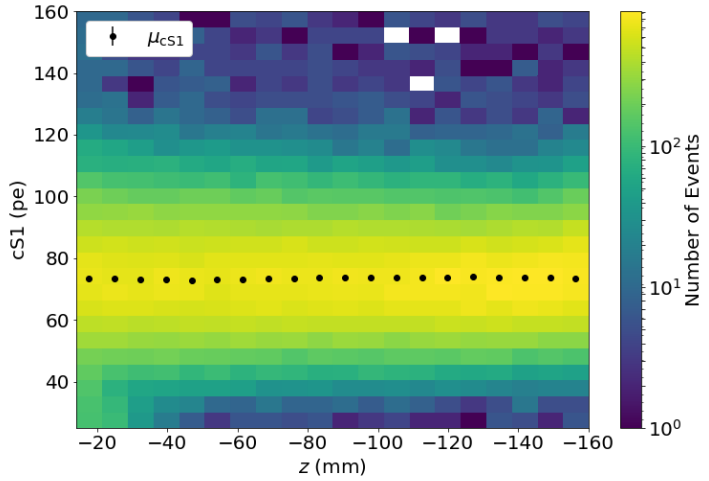

(b) After LCE-correction.

Figure 4.12 – S1 depending on the drift time. The means were obtained via guassian fits to every z-slice.

The S1-correction for LCE effects is then calculated via

$$cS1 = S1(z) \cdot \frac{\text{norm}}{\mu_{\text{S1}}} \tag{4.4.1}$$

with the corrected signal cS1. The norm is set to the sum of all μ_{S1} divided by the number of z-slices. The $(z, \mathrm{S1})$ and $(z, \mathrm{cS1})$ distributions are shown in figure 4.12. Interactions originating from the top differ significantly from bottom interactions. After the correction, the S1 distributions lie in a constant line.

Monte-Carlo simulations of the LCE in the Münster dual-phase TPC have been conducted in the scope of a bachelors thesis [3]. Among other things, these simulations assumed 178 nm photons, 100 cm photon absorption length and 14 functional PMTs. As the current setup operates with 13 PMTs, the simulations were updated by L. Althüser, so they could be compared with data. The measured LCE is normed to its mean value in order to compare it with the simulated relative LCE. As figure 4.13 illustrates, simulation and experiment show a remarkable consistency. Deviations occur only at deep interactions near the bottom PMTs, where geometry effects are stronger.

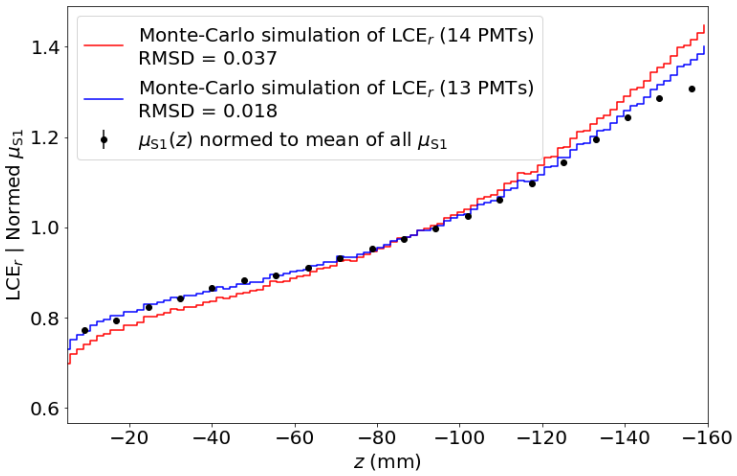

Figure 4.13 – Monte-Carlo simulations of the relative LCE of the Münster TPC for 13 PMTs (current setup) and 14 PMTs are shown. The normed μ_{S1} position for every z-slice is shown for comparison.

4.5 S2-Correction

The charge collection efficiency in liquid xenon strongly depends on the fraction of electronegative impurities like O_2. These impurities absorb electrons with a mean electron lifetime τ_{e^-}, as stated in chapter 2.2. Further, the extraction field strength influences the total charge collection, but this effect is fixed and not corrected here. A correction of the electron absorption is presented in the following section with ^{83m}Kr and ^{137}Cs data that prepared as described in section 4.1 and 4.2.

Similar to the S1-correction in the previous section, the detector volume is seperated into drift time slices. Here, drift time slices are favored over z-slices, since it is more natural to measure the electron lifetime on a time scale. The electron lifetime is estimated from an exponential fit to the mean S2 values of the drift time slices.

To bypass saturation effects, the S2 from the top PMTs is ignored. Only the bottom PMTs contribute to the S2 (marked by $S2_b$). The dependence of $S2_b$ on the drift time is investigated. For both, ^{83m}Kr and ^{137}Cs, the mean $S2_b$ of the drift time slices are fitted with a Gaussian distribution via the `migrad` function as described in the previous section. The mean positions for ^{83m}Kr and ^{137}Cs are shown in figure 4.14, fitted with an exponential function, where the decay time corresponds to the electron lifetime.

The electron lifetime τ_{e^-} is increasing over time: From $\tau_{e^-} = (358.4 \pm 9.8)\,\mu$s, measured in the combined ^{83m}Kr datasets at the beginning of the data taking to $\tau_{e^-} = (947.8 \pm 70.3)\,\mu$s after 5 days, measured in the ^{137}Cs dataset, as shown in figure 4.15. An increase was expected because of the continuous purification of the xenon content. It is not clear, wether or when the electron lifetime has reached a plateau during the measurements. However, it is crucial for the energy calibration to correct the $S2_b$ of the background dataset as well. The simplest approximation, since the position of the τ_{e^-}-plateau is unknown, is a linear approximation of the electron lifetime from the ^{83m}Kr to the ^{137}Cs datasets. This leads to an estimated electron lifetime $\tau_{e^-,\mathrm{est}} = 525\,\mu$s during the background data taking.

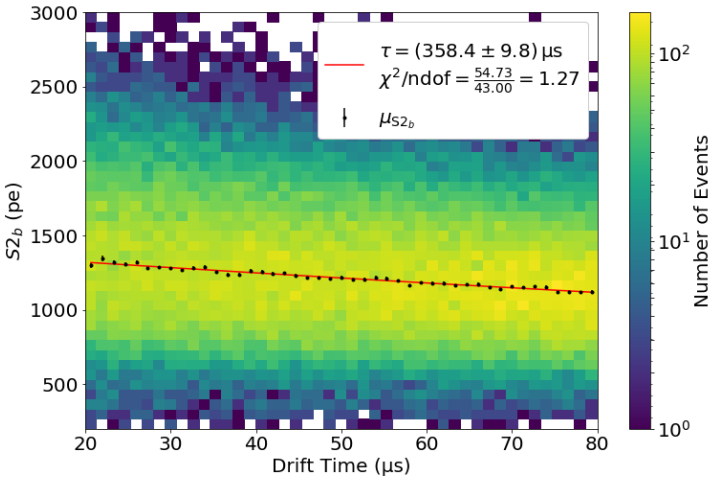

(a) $S2_b$ depending on the drift time for the ^{137}Cs dataset.

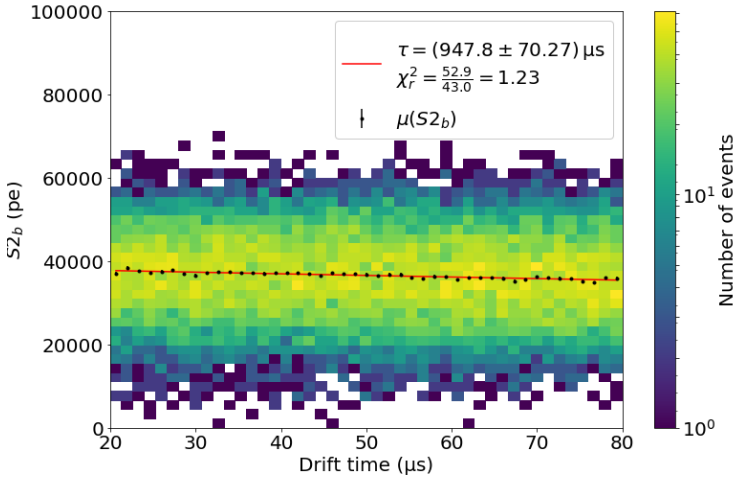

(b) $S2_b$ depending on the drift time for the ^{137}Cs dataset.

Figure 4.14 – Electron lifetime fits for the ^{83m}Kr and ^{137}Cs data.

The electron lifetime of the XENON1T experiment as well showed an increase throughout its dark matter search runs with a highest documented value of $\tau_{e^-} \simeq 650\,\mu s$ [13]. The electron lifetime in the Münster TPC is significantly larger than

the electron lifetime in the XENON1T TPC. That is due to the smaller volume and, therefore, larger purification rate of the Münster TPC, although the efforts to minimize impurities in the XENON1T experiment were far greater by extremely careful screening of its components. However, as a consequence of the saturation described in section 4.2, the electron lifetime for ^{137}Cs signals and, therefore, the electron lifetime of the background dataset is likely to be overestimated, but this needs further investigation.

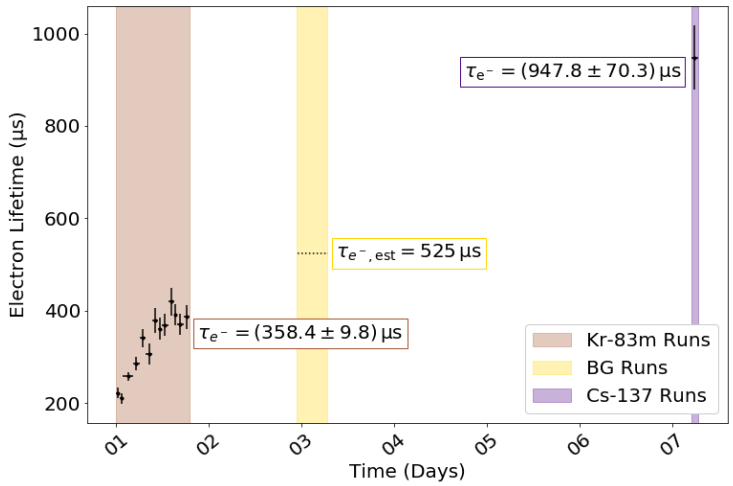

Figure 4.15 – Temporal development of the electron lifetime throughout the measurements. The ^{83m}Kr data is composed of 13 consecutive datasets that were combined for the analysis. The electron lifetime calculated for each of these datasets increases in time. The value for the background dataset is approximated linearly.

Eventually, the S2s are corrected to

$$cS2 = S2 \cdot e^{t/\tau_{e^-}}, \tag{4.5.1}$$

where cS2 is the corrected S2, t the drift time and τ_{e^-} is the electron lifetime.

The signals before and after the S1 and S2 correction are shown in figure 4.16. The ^{83m}Kr spectrum shows a compression in S1 and S2 direction and is more centered after the corrections. In the ^{137}Cs spectrum after corrections, the full-absorption peak is also more centered and clearly distinguishable from the

Compton-continuum.

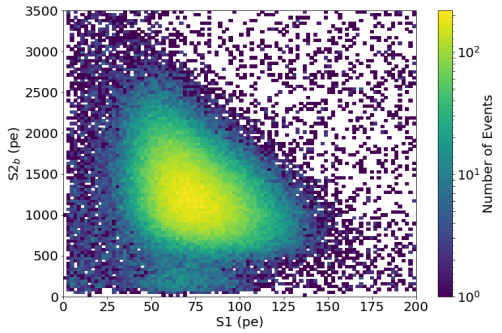

(a) ^{83m}Kr spectrum before corrections.

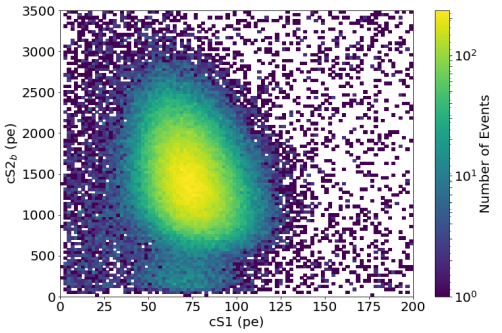

(b) ^{83m}Kr spectrum after corrections.

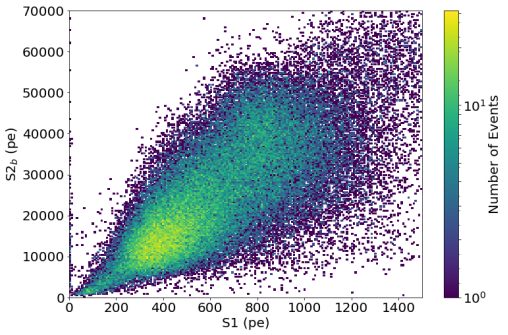

(c) ^{137}Cs spectrum before corrections.

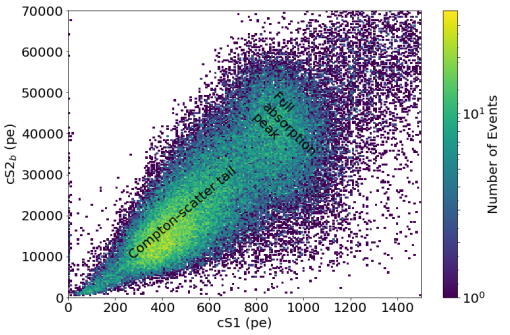

(d) ^{137}Cs spectrum after corrections.

Figure 4.16 – S2 depending on S1 for ^{83m}Kr and ^{137}Cs before and after the S1 and S2 correction.

5 Energy Calibration

The two ways of obtaining an energy calibration of liquid xenon dual-phase TPCs with either several energies or with a single energy and determination of the anti-correlation angle are shown in chapter 2.2. In general, it is preferable to use a variety of calibration sources and acquire informations about the detector response at different energy ranges, although the anti-correlation angle of light and charge yield can be exploited to calculate the energy from only one source. Both methods are applied and compared for the Münster TPC with ^{83m}Kr and ^{137}Cs in the following chapter.

5.1 Light and Charge Yield of ^{83m}Kr Signals

The low-energy calibration is achieved with ^{83m}Kr. In contrast to the cuts on the ^{83m}Kr signal in chapter 4.2, it is important here to match a signal population with its corresponding energy. The 32.1 keV and 41.5 keV signals of the ^{83m}Kr decay are extracted via specific data cuts.

Specific Data Cuts

To distinguish the 32.1 keV and 41.5 keV signals, specific data cuts had to be developed individually for both signatures in addition to the data quality cuts. All applied data cuts are listed in table 5.1. The remaining populations are shown in figure 5.1.

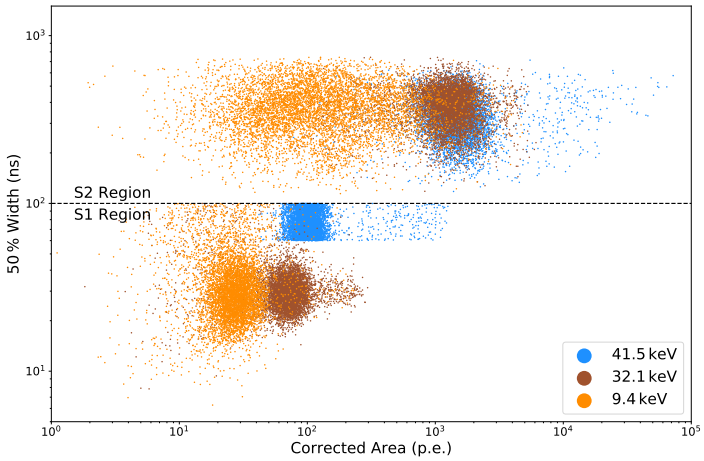

Figure 5.1 – The S2 width depending on the corrected area shows the remaining populations of the ^{83m}Kr data after application of the dedicated cuts. The 9.4 keV $S2_1$ signature is less centered. Small S2s have a larger risk of being fractured, because the clustering is not optimized for them. That is presumably the reason for the smeared out $S2_1$ population of the 9.4 keV signal. Therefore, they are not used for the energy calibration.

32.1 keV Signal

To ensure that the main S2 corresponds to 32.1 keV and is not mixed with the 9.4 keV signal, a second S2 – smaller than the first and measured after it – is demanded. This second S2 signal is identified as the 9.4 keV signal when it is larger than 50 pe and otherwise dismissed to exclude single electron signals. The background mostly consists of signals that are larger than the ^{83m}Kr population. S2s larger than 15000 pe and S1s larger than 250 pe are far greater than any ^{83m}Kr signal and, so, they are cut. To further minimize the remaining number of background events, the ratio of the largest S1, corresponding to the 32.1 keV signal, and the largest other S1, corresponding to the 9.4 keV signal, is demanded to be smaller than 15. The ratio $32.1/9.4 \approx 3.4$ that would be expected without uncertainties is thereby included. Background events like random coincidences do not have such a constraint on their S1 ratio and are efficiently reduced.

Table 5.1 – Data cuts used to extract the 32.1 keV and 41.5 keV signatures of the ^{83m}Kr decay.

Energy	Data Cut	Remaining
32.1 keV	S1 prior to S2	95 %
	$S1_1$ prior to S2	28 %
	$S2_1 > 50$ pe	8.9 %
	S2 < 15000 pe	0.48 %
	S1 < 250 pe	0.29 %
	$S1/S1_1 < 15$	0.24 %
	S2 width cut	0.16 %
	S1 area fraction top cut	0.15 %
41.5 keV	S1 prior to S2	95 %
	$S1_1$ prior to S2	1.6 %
	S1 width > 60 ns	1.6 %
	No $S2_1$ OR $S2_1 < 50$ pe	1.6 %
	20 pe $< S1 < 1000$ pe	0.62 &
	S2 width cut	0.55 %
	S1 area fraction top cut	0.53 %

41.5 keV Signal

For the 41.5 keV signal, a weakness of the current signal processing setting is exploited: S1s occuring less than 30 ns after another cannot be distinguished in time. [1] No signal population was found at temporal widths greater than 60 ns in the background data, whereas in the ^{83m}Kr data such a population is measured. Summed waveforms of the S1s in this region show a clear double peak structure revealing that they are merged S1s. So, it is concluded that these merged S1s have the combined energy of both ^{83m}Kr decays of 9.4 keV + 32.1 keV. Due to the small time difference of the merged S1s and the naturally high width of S2s, the corresponding S2 is inevitably merged from 9.4 keV and 32.1 keV if the original energy deposition stems from ^{83m}Kr. Therefore, to reduce random coincidences by energy depositions at different positions in the detector, all events that come with

[1] In principle, the data processor can be adjusted to other separation times. This would have further impacts like changing the S1 and S2 area and width.

more than a single S2 are cut.

The remaining S1 and S2 populations with their assigned energies are shown in a scatter plot in figure 5.1 of S2 width depending on S1 or S2 area.

Light and Charge Yield

The (S1, S2) spectra that remain after the specific data cuts for both extracted energy lines are shown in figure 5.2. The light and charge yield are computed from a bivariate gaussian fit on the 32.1 keV and 41.5 keV ellipses, each obtained by minimizing the χ_r^2 of the fit. The light and charge yields are shown in table 5.2. A decrease in light yield and an increase in charge yield is expected from the anti-correlation properties with higher energies [25]. Hence, the 41.5 keV signal seems inconsistent because the evolution of its light and charge yields is vice versa. However, it is a composite signal of 9.4 keV and 32.1 keV. Therefore a larger light yield and lower charge yield are measured than expected from a 41.5 keV signal of a single energy deposition, resolving this contradiction.

Table 5.2 – Light yield L_y and charge yield C_y of the 32.1 keV and 41.5 keV signatures of the ^{83m}Kr decay.

Energy	L_y	C_y
32.1 keV	2.25 ± 0.01 pe/keV	41.4 ± 0.2 pe/keV
41.5 keV	2.42 ± 0.01 pe/keV	35.7 ± 0.2 pe/keV

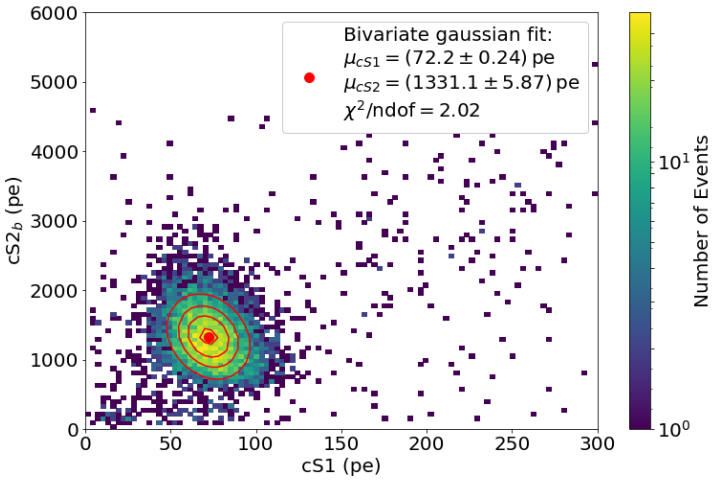

(a) 32.1 keV population.

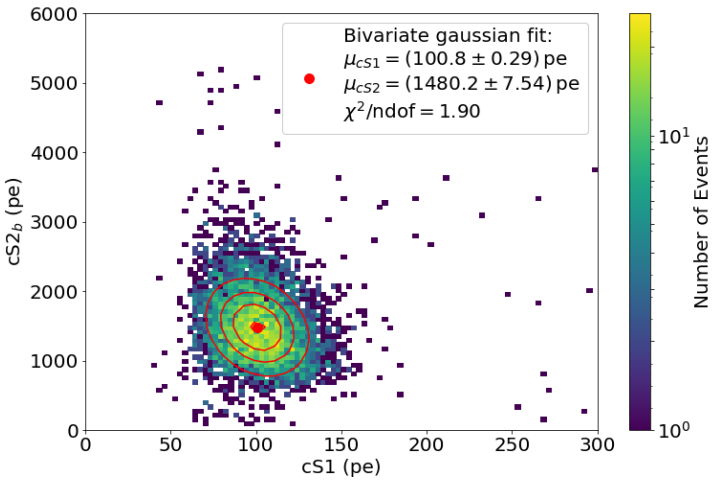

(b) 41.5 keV population.

Figure 5.2 – S2$_b$ dependence of S1 for the 32.1 keV and 41.5 keV ^{83m}Kr data, each fitted with a bivariate gaussian to calculate the mean position of S1 and S2$_b$.

5.2 Light and Charge Yield of ^{137}Cs Signals

The ^{137}Cs source was placed about 1 m away from the TPC. The resulting event rate, including background, was 336.1 Hz. The 661.7 keV full-aborption peak comes with an overlapping compton-scatter tail. Extraction of the properties of the full absorption peak is therefore non-trivial. Additionally, large parts of the background spectrum are located in the region lower than 661.7 keV. By subtracting a background spectrum - taken beforehand with an event rate of 163.3 Hz - from the ^{137}Cs spectrum, the remaining spectrum predominantly consists of ^{137}Cs events and extracting the correct properties of the full-absorption peak becomes possible.

Specific Data Cuts and Background Correction

The ^{137}Cs spectrum and the to be subtracted background spectrum are shown in figures 5.3a and 5.3b. The data cuts described in section 4.2 and the data quality cuts described in section 4.1 are applied. The background data is treated with the same set of data cuts. The data cuts and the remaining fraction after cut application are summarized in table 5.3.

Table 5.3 – Specific data cuts used to extract the ^{137}Cs signal.

Dataset	Data Cut	Remaining
^{137}Cs	No $S2_1$ or $S2_1 < 0.1$S2	78 %
	No $S1_1$	22 %
	10 μs < drift time < 90 μs	14 %
	S2 middle PMT cut	5.1 %
	S2 width cut	4.4 %
	S1 area fraction top cut	4.2 %
Background	No $S2_1$ or $S2_1 < 0.1 \cdot$ S2	79 %
	No $S1_1$	19 %
	10 μs < drift time < 90 μs	11 %
	S2 middle PMT cut	4.5 %
	S2 width cut	3.9 %
	S1 area fraction top cut	3.8 %

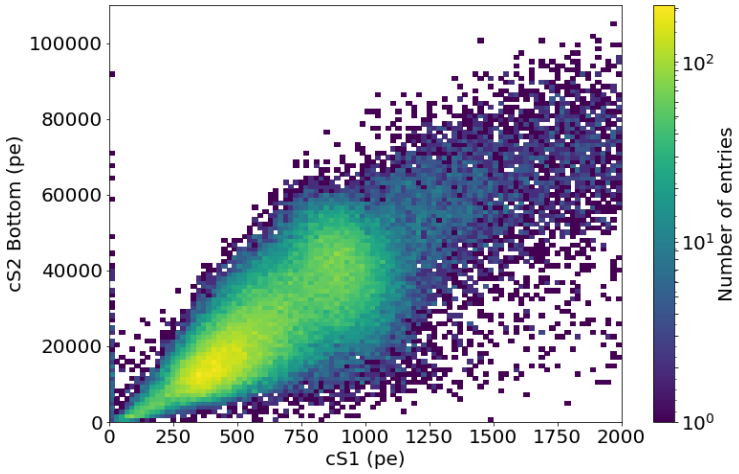

(a) Spectrum of the ^{137}Cs data.

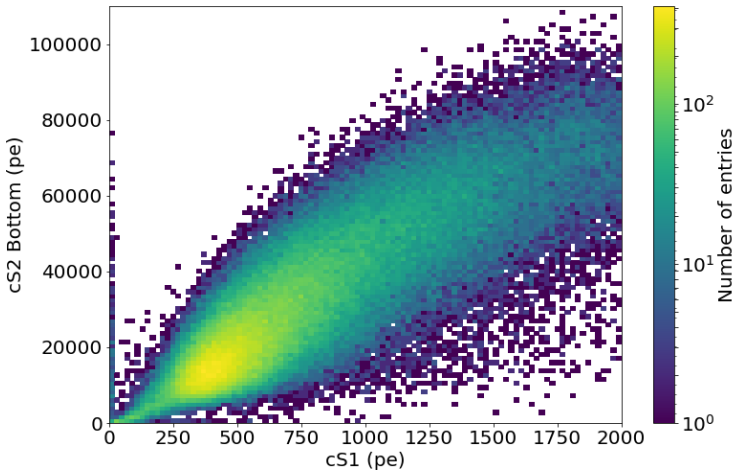

(b) Background spectrum.

Figure 5.3 – Spectra of ^{137}Cs and background data after application of the specific cuts of table 5.3.

The applied cuts reduce the rate of events in the measurement consisting of ^{137}Cs signals and background to $r_{\mathrm{meas,Cs}} = 13.3\,\mathrm{Hz}$. The rate of events in the background measurement is reduced to $r_{\mathrm{meas,BG}} = 5.8\,\mathrm{Hz}$. The total measurement

times of both datasets is different. This has to be accounted for by normalizing each spectrum to its measurement time. Additionally, an effective dead time $T_{d,\text{eff}}$ needs to be considered, with the effective dead time calculated via

$$r_{\text{real}} = \frac{r_{\text{meas}}}{1 - r_{\text{meas}} T_{d,\text{eff}}}. \tag{5.2.1}$$

The dead time measured in section 4.2 cannot be used for correcting the signals, because the applied cuts affect the datasets differently (see table 5.3). Therefore, a very similar procedure is used to determine an effective dead time correction that additionally incorporates effects of the data cuts as follows. The S1 spectra are normed to the measurement time and divided by $(1 - r_{\text{meas}} T_{d,\text{eff}})$ with their respective rate. The end range of the ^{137}Cs spectrum is expected to have the same shape as the background spectrum, since no energy higher than the full-absorption peak is emitted from ^{137}Cs. The ^{137}Cs spectrum end range is subtracted from the background spectrum end range with variable $T_{d,\text{eff}}$. The minimum mean square deviation of the outcome in dependence of $T_{d,\text{eff}}$ corresponds to the effective detector dead time $T_{d,\text{eff}} = 0.0105\,\text{s}$ that is not directly connected to the detector dead time calculated in 4.2 due to the application of data cuts. The S1 spectra before and after the effective dead time correction are shown in figure 5.4. Finally, the normalized (S1,S2) spectrum of the background is subtracted from the ^{137}Cs spectrum considering the effective dead time.

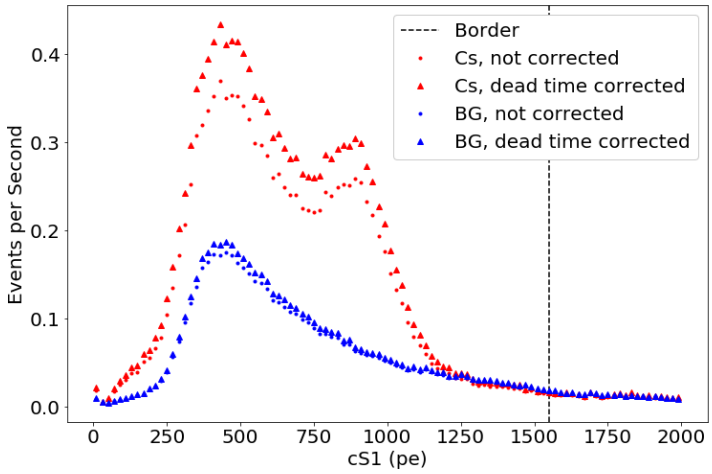

Figure 5.4 – S1 spectrum of background and ^{137}Cs data, normalized to the respective measurement time, before and after application of the effective dead time correction. The spectra were compared for S1s larger than the drawn border to minimize the influence of γ-rays from ^{137}Cs.

Light and Charge Yield

Extracting the light yield L_y and charge yield C_y from the ^{137}Cs signal is non-trivial in contrast to the ^{83m}Kr signal. Especially for small TPCs the Compton-scattering region is relatively big and smeared out into the full-absorption peak and the Compton-edge, as figure 5.3a illustrates. Fitting an ellipse in the background-subtracted spectrum was not successfull due to the large detector background and the broad Compton-scattering region. A way to handle this is to find the anti-correlation angle θ and to keep θ constant in the ellipse fit. For this purpose, equation 2.2.6 is used to calculate a combined scale along the anti-correlation axis of the peak, but the proportional factor ν is ignored for now. The resulting spectrum is expected to show the maximum peak-to-valley ratio and the minimum resolution of the Cs-peak for θ in contrast to angles which do not correspond to the correct anti-correlation axis. The sum of two Gaussian curves is fitted to the resulting projection for a range of different angles. For the purpose of finding the mean and width of the second gaussian peak and the peak to valley ratio the underlying Compton-scattering tail is fitted as gaussian distribution. There is no

intention to make a statement about the Compton-scattering region. Therefore, the gaussian fit is favored over less practicable approaches. The peak to valley ratio P/V is calculated, as well as the resolution $\mathrm{Res}(\theta)$ of the second Gaussian distribution as signal width divided by mean position. Maximization of the peak to valley ratio and minimization of the resolution leads to $\theta = 89.56\,^\circ$, as figure 5.5 shows.

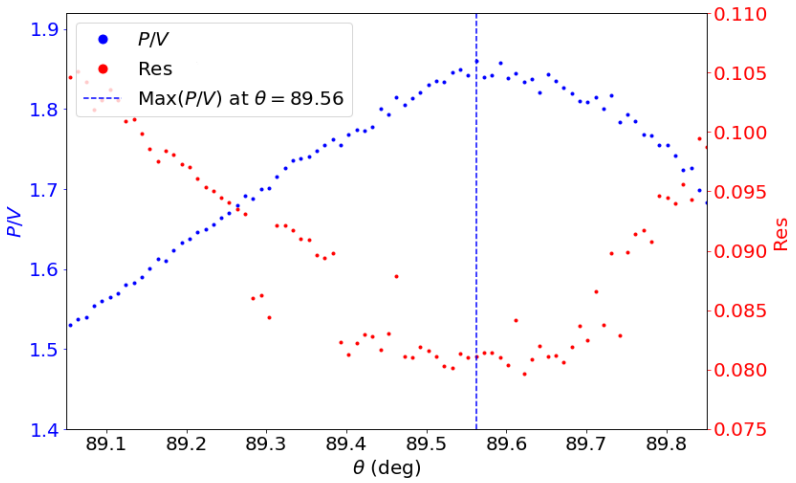

Figure 5.5 – Peak to valley ratio P/V and resolution $Res(\theta)$ depending on the anti-correlation angle. They are determined via two gaussian fits to the spectrum for each successive iteration over theta.

The maximum P/V valley is not clearly determined, but there is no direct functional relation of P/V and θ. Therefore, the error of θ is assumed to be $\Delta\theta = 0.1\,^\circ$. The spectrum obtained with this anti-correlation angle is shown in figure 5.6.

With knowledge of the anti-correlation angle θ, another attempt at extracting the light and charge yield by fitting an ellipse to the $(\mathrm{S1}, \mathrm{S2})$ spectrum is made, where θ is kept constant. The spectrum is shown in figure 5.7. The fit range is set narrow around the full-absorption peak and the Compton-scattering area is fitted by a second ellipse with its center outside of the fit range. To find the mean S1 and S2 of the full-absorption ellipse, the underlying Compton-scattering region is fitted via a bivariate gaussian distribution. This is sufficient since it is not the aim

to make physical statements about this region. Eventually, this procedure leads to

$$L_{y,661.7} = \frac{(904 \pm 3)\,\mathrm{pe}}{661.7\,\mathrm{keV}} = (1.366 \pm 0.004)\,\mathrm{pe/keV} \tag{5.2.2}$$

$$C_{y,661.7} = \frac{(41755 \pm 290)\,\mathrm{pe}}{661.7\,\mathrm{keV}} = (63.1 \pm 0.4)\,\mathrm{pe/keV}. \tag{5.2.3}$$

The light yield of the XENON100 TPC at 0.53 kV/cm drift field was between 1.57 pe/keV [7] and (1.74 ± 0.04) pe/keV, where the charge yield was (368.44 ± 0.45) pe/keV [41]. The light yield measured in this work is slightly smaller than that measured with the XENON100 detector that was equipped with 242 PMTs and 62 kg liquid xenon in the target volume [8]. However, the charge yield in the Münster TPC suffers from saturation effects, low electron extraction efficiency and presumably liquid level instablities. This is reflected in the low charge yield compared to the charge yield measured with the XENON100 detector for 661.7 keV γ-rays.

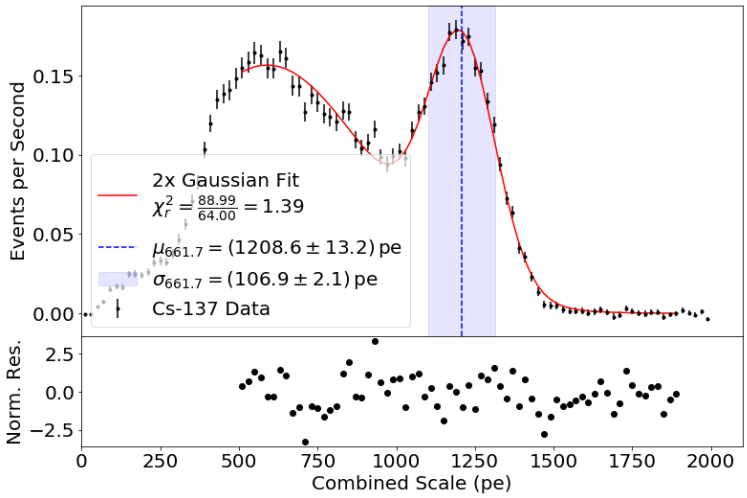

Figure 5.6 – Combined S1 and S2 spectrum of ^{137}Cs, where the backround is subtracted. The combined scale is obtained from equation 2.2.6 with $\theta = 89.56\,°$, where the normalization factor ν is ignored.

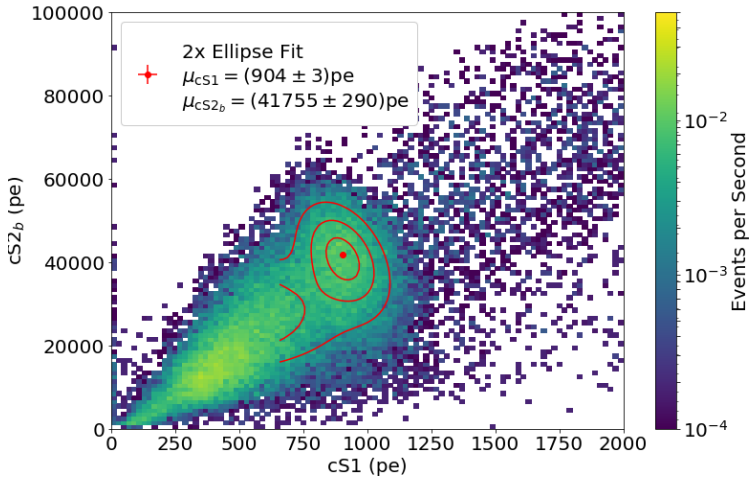

Figure 5.7 – ^{137}Cs spectrum, where the background spectrum was subtracted. A twofold bivariate gaussian fit with fixed angle θ is used to extract the mean S1 and S2 of the 661.7 keV full-absortion peak.

5.3 Energy Calibration with ^{83m}Kr and ^{137}Cs

The measured light and charge yields of both sources are used in this section to calculate an energy scale that combines direct and proportional scintillation via equation 2.2.5. The combined energy will also be calculated with equation 2.2.6 from a single source and the anti-correlation angle of its light and charge signals.

Combined Energy Calibration from ^{83m}Kr and ^{137}Cs

The linear dependency of the charge yield on the light yield is exploited for all measured energies of 32.1 keV, 41.5 keV and 661.7 keV to calculate the energy scale. The photon detection efficiency $g_{1,\mathrm{Kr+Cs}} = (0.0531 \pm 0.0003)\,\mathrm{pe/ph}$ and the charge amplification factor $g_{2,\mathrm{Kr+Cs}} = (1.31 \pm 0.01)\,\mathrm{pe}/e^-$ are determined from a linear fit of equation 2.2.5 to the measured light and charge yields, as illustrated in figure 5.8 (blue dashed line).

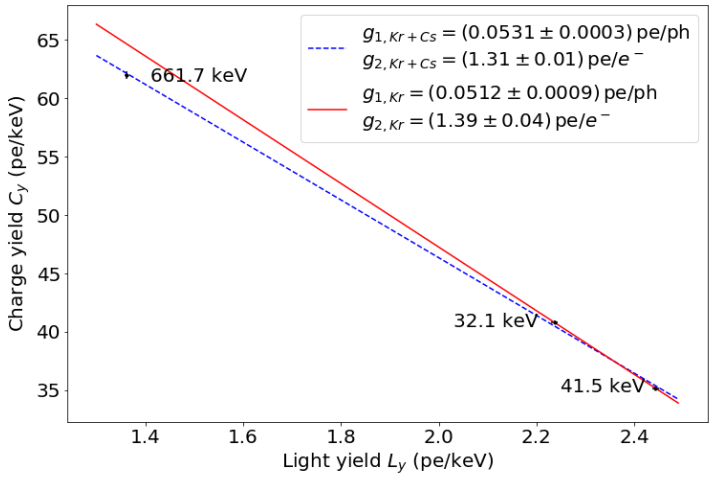

Figure 5.8 – Charge yield in depence of the light yield, fitted with equation 2.2.5 for ^{83m}Kr (red line) and ^{83m}Kr and ^{137}Cs (blue dashed line).

The reconstruction of the energy for each of these signals, as shown in figure 5.9, lead to reconstruction of the energy with 1.4 %, 0.5 % and 1.2 % for 32.1 keV, 41.5 keV and 661.7 keV discrepancy to the intended mean position. The energy resolutions $\mathrm{Res}(E) = \sigma(E)/\mu(E)$ are

$$\mathrm{Res}(32.1\,\mathrm{keV}) = \frac{(4.90 \pm 0.08)\,\mathrm{keV}}{(32.54 \pm 0.08)\,\mathrm{keV}} = (15.1 \pm 0.2)\,\%, \tag{5.3.1}$$

$$\mathrm{Res}(41.5\,\mathrm{keV}) = \frac{(6.09 \pm 0.07)\,\mathrm{keV}}{(41.73 \pm 0.09)\,\mathrm{keV}} = (14.6 \pm 0.2)\,\%, \tag{5.3.2}$$

and

$$\mathrm{Res}(661.7\,\mathrm{keV}) = \frac{(96.7 \pm 4.8)\,\mathrm{keV}}{(653.7 \pm 4.2)\,\mathrm{keV}} = (14.8 \pm 0.7)\,\%, \tag{5.3.3}$$

where the two former peaks are fitted via Gaussian functions and the latter is fitted via the sum of two Gaussian functions to describe the peak and the influence from its underlying Compton-scattering region to it.

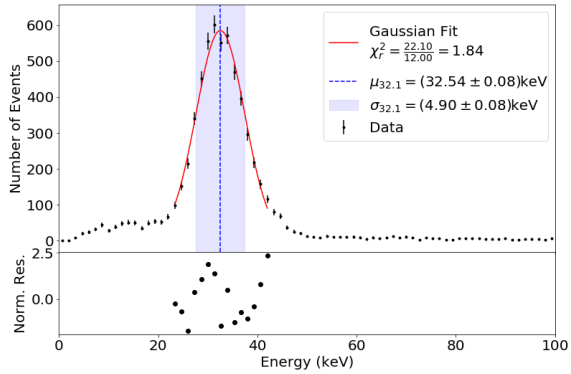

(a) ^{83m}Kr spectrum of 32.1 keV, fitted with a Gaussian function.

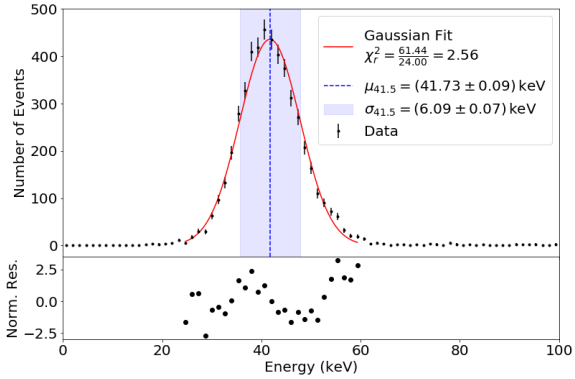

(b) ^{83m}Kr spectrum of 41.5 keV, fitted with a Gaussian function.

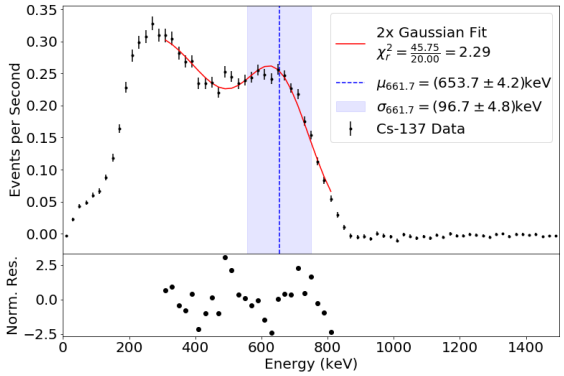

(c) Spectrum of ^{137}Cs, fitted with the sum of two gaussian functions.

Figure 5.9 – The energy spectra for the ^{83m}Kr and ^{137}Cs data, where $g_{1,\mathrm{Kr+Cs}}$ and $g_{2,\mathrm{Kr+Cs}}$ are used in equation 2.2.3 to determine the combined scale.

However, the full-absorption peak of ^{137}Cs in figure 5.9c is not clearly separated from the Compton scattering region, in contrast to the stronger separation shown in the spectrum in figure 5.6. Thus, the calibration over a broad range of energies is not optimal and indicates a non-linear detector response for different energies. An explanation for the non-linearity is found in the detector response for S2s of ^{137}Cs. As expected from XENON100, S2s in the top PMT array cause saturation, which is why they are not used for the energy calibration at all [25]. First investigations of the single channel response of the PMT channels in the bottom array show saturation, too, as shown in figure 4.9. Therefore, the ^{137}Cs spectrum needs a saturation correction to be comparable to the ^{83m}Kr spectra. Additionally, despite the slow control data showing constant pressure and temperature, the ^{137}Cs dataset was recorded about five days after the ^{83m}Kr measurements. Small changes in the liquid level from the ^{83m}Kr to the ^{137}Cs datasets, as discussed in section 3.2, might have altered the electron extraction and charge ampflification. In this line of argument, only the 32.1 kev and 41.5 keV signals remain to construct the combined energy scale with this method that is shown in figure 5.8 (red line) with

$$g_{1,\mathrm{Kr}} = (0.0512 \pm 0.0009)\,\mathrm{pe/ph} \tag{5.3.4}$$

and

$$g_{2,\mathrm{Kr}} = (1.39 \pm 0.04)\,\mathrm{pe}/e^{-}. \tag{5.3.5}$$

The resulting spectra are shown in figure 5.10. Their mean positions show discrepancies to the intended energies of 0.8 % and 1.1 % for the 32.1 keV and 41.5 keV line positions and energy resolutions of

$$\mathrm{Res}(32.1\,\mathrm{keV}) = (15.3 \pm 0.2)\,\% \tag{5.3.6}$$

and

$$\mathrm{Res}(41.5\,\mathrm{keV}) = (14.1 \pm 0.2)\,\%. \tag{5.3.7}$$

The resolution of the 32.1 keV peak is in agreement with the previous value, whereas the 41.5 keV peak resolution has slightly improved.

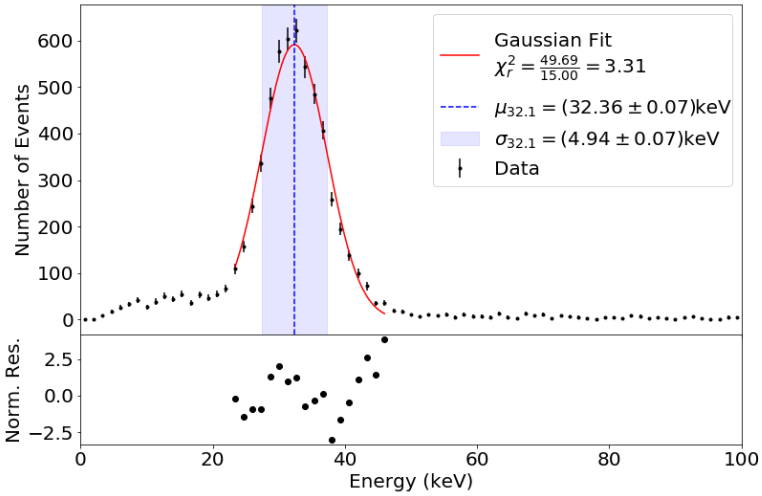

(a) ^{83m}Kr spectrum of 32.1 keV, fitted with a Gaussian function.

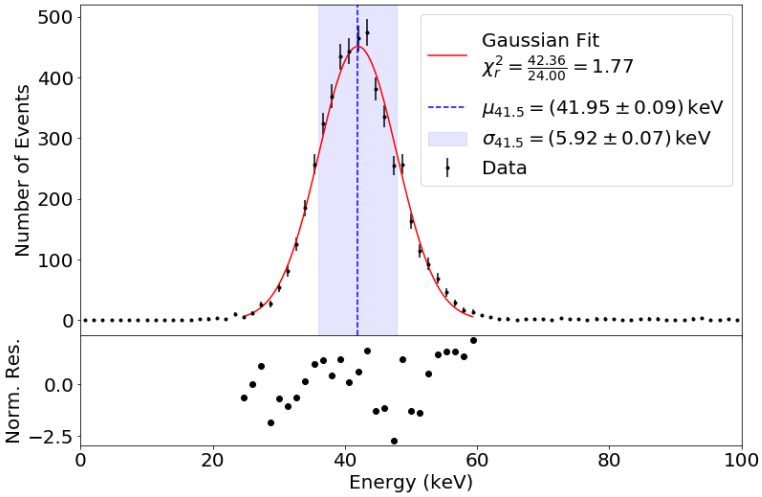

(b) ^{83m}Kr spectrum of 41.5 keV, fitted with a Gaussian function.

Figure 5.10 – The energy spectra for the ^{83m}Kr data, where $g_{1,\mathrm{Kr}}$ and $g_{2,\mathrm{Kr}}$ are used in equation 2.2.3 to determine the combined scale.

Combined Energy Calibration from ^{137}Cs

Despite saturation effects and possibly liquid level changes, an energy calibration, due to the non-linearity only valid for the ^{137}Cs signature, by using the anti-correlation angle θ of the 661.7 keV full-absorption peak. Equation 2.2.6 is used to determine the $g_{1,\theta}$ and $g_{2,\theta}$ factors for the detector via

$$g_{1,\theta} = \frac{\nu \cdot W \cdot (\sin\theta + \cos\theta)}{\sin\theta} = (0.0252 \pm 0.0004)\,\mathrm{pe/ph} \tag{5.3.8}$$

and

$$g_{2,\theta} = \frac{\nu \cdot W \cdot (\sin\theta + \cos\theta)}{\cos\theta} = (3.28 \pm 0.74)\,\mathrm{pe}/e^{-}, \tag{5.3.9}$$

with the effective energy $W = 13.7\,\mathrm{eV}$ for generation of a single photon or electron-ion pair, anti-correlation angle $\theta = (89.56 \pm 0.1)^\circ$ and normalization factor $\nu = (1.827 \pm 0.003)\,\mathrm{pe/keV}$. The latter is drawn from the mean position $\mu_{661.7} = (1208 \pm 2)\,\mathrm{pe/keV}$ of the second Gaussian peak in the combined scale spectrum in figure 5.6 divided by 661.7 keV. These $g_{1,\theta}$ and $g_{2,\theta}$ differ significantly from $g_{1,\mathrm{Kr+Cs}}$ and $g_{2,\mathrm{Kr+Cs}}$, as calculated in the previous section, and cannot be explained by saturation effects alone: Saturation corrections would lead to a larger charge yield and, therefore, a larger anti-correlation angle θ. This would increase $g_{2,\theta}$, but would barely alter $g_{1,\theta}$. Further measurements are required to analyze an influence of the liquid level on $g_{1,\theta}$ and $g_{2,\theta}$.

Eventually, the resulting energy spectrum in figure 5.11 shows a full-absorption peak at 661.7 keV with Compton-scattering antecedently. Compared to the spectrum shown in the previous section, the 661.7 keV peak is clearly distinguishable. The mean position and standard deviation from the second Gaussian fit in figure 5.6 are used to determine the energy resolution:

$$\mathrm{Res}(661.7\,\mathrm{keV}) = (8.8 \pm 0.2)\,\%. \tag{5.3.10}$$

The resolution has significantly improved by utilization of the anti-correlation angle in contrast to the resolution of this line in the previous section.

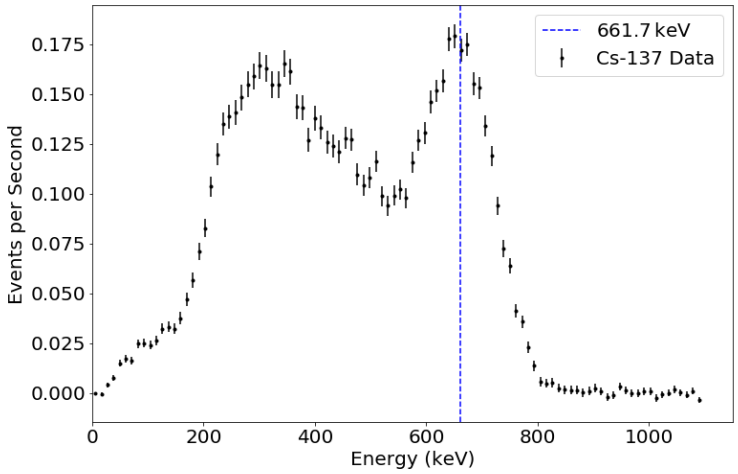

Figure 5.11 – The ^{137}Cs spectrum shown in 5.6 is here normalized with ν to express the actual energy.

Discussion of the Energy Calibration

The energy calibration for this detector uses two in principle equivalent methods, that however lead to inconsistent results for the energy resolution at 661.7 keV. This is due to the saturation effects and presumably a slight variation of the liquid level over time. The energy resolution obtained with S1-only or S2-only readout is much lower, as shown in figure 5.12. With the combined scale, the energy resolution is improved and, as anticipated from equation 2.2.8, can be described by a $\sqrt{1/E}$ law.

For comparability with other dual-phase liquid noble gas TPCs, the 122 keV γ-line of ^{57}Co is used as reference. However, due to the good self-shielding capabilities of xenon, the 122 keV photons cannot penetrate the inner volume of bigger TPCs and thus are modeled via NEST. As a model for scintillation and ionization of liquid xenon in a drift field, the NEST predictions are scaled to the actual detector response via g_1 and g_2. The resulting NEST curves are calculated in figure 5.13 with $g_{1,\mathrm{Kr}}$ and $g_{2,\mathrm{Kr}}$ of the $^{83\mathrm{m}}$Kr energy calibration. ^{137}Cs was not used because of the unresolved saturation effects in the 661.7 keV signal. All three data points are in good agreement with or near to the predictions of the model. The 122 keV

reference energy has a light yield of $L_{y,122} = (1.92 \pm 0.08)\,\mathrm{pe/keV}$ and a charge yield of $C_{y,122} = (49.4 \pm 4.0)\,\mathrm{pe/keV}$. The 41.5 keV point from the ^{83m}Kr measurement is shown, but the prediction of NEST should not be considered very reliable there, since it is a composite signal and therefore not subject to the assumptions of the NEST model on a microscopical level.

Refinement of the predictions of the NEST model for the Münster TPC with more calibration sources should be considered, since the presented results are currently solely drawn from the low-energy source ^{83m}Kr. It is expected that, after saturation correction and stability enhancement, a linear combined energy scale that is valid for the energy range from 32.1 keV to 661.7 keV can be presented.

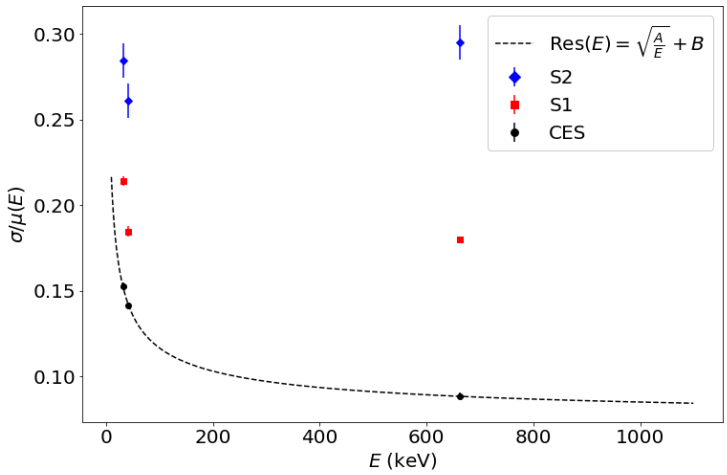

Figure 5.12 – Detector resolution for S1, S2 and the combined energy scale depending on energy. The S1 and S2 spectra that were used to calculate the resolution are shown in the appendix at A.2 and A.3. The S2 spectrum at 661.7 keV did not have a clearly separated full-absorption peak and so, the error is presumably underestimated.

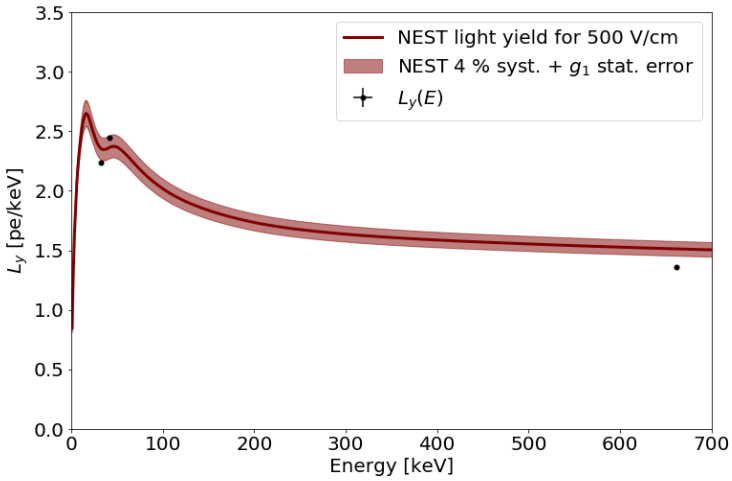

(a) Light yield L_y.

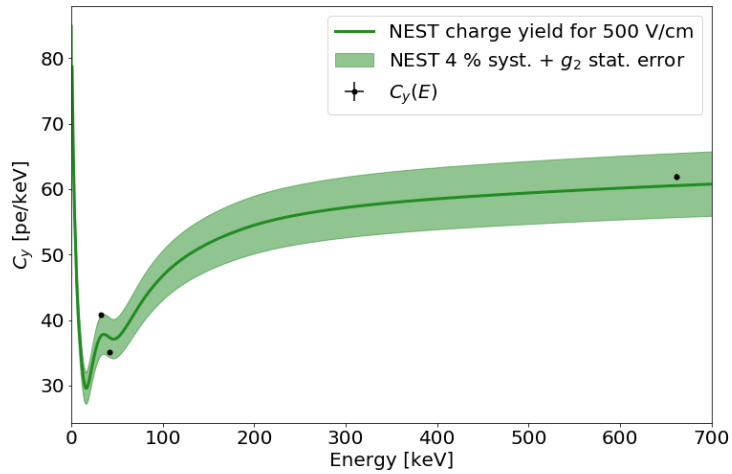

(b) Charge yield C_y.

Figure 5.13 – Light and charge yield calculated from $g_{1,\mathrm{Kr}}$ and $g_{2,\mathrm{Kr}}$ with NEST and light and charge yield measured within this work for $^{83\mathrm{m}}$Kr and ^{137}Cs signatures. Python code for the NEST curves was made available by C. Wittweg.

6 Conclusion

Significant steps were made throughout this work towards a deeper understanding of the Münster TPC. The energy calibration of the detector system was succesfully obtained with two different radioactive sources. Routines for data preparation, analysis and energy calibration were developed in `python`. During the process, the settings for the PAX data processor were optimized to reliably distinguish between S1s and S2s.

The interaction depth reconstruction was implemented, which is a first step towards the 3D position reconstruction of interactions. The implementation of (x, y)-position reconstruction via machine learning algorithms that could be trained with the homogeneously distributed ^{83m}Kr decay signatures should be attempted in future and would enable the full potential of the Münster TPC.

Depth-dependent corrections of S1s and S2s were performed, including a successful measurement of the electron lifetime and its temporal behaviour. Further, it was confirmed experimentally that Monte-Carlo simulations by L. Althüser describe the z-dependence of S1s with remarkable accuracy. The results of the comparison of simulation and data give reason to further investigate on Monte-Carlo simulations of the Münster TPC.

The energy calibration of the detector was obtained by combining light and charge readout to achieve a higher resolution. It was shown that the energy resolution of the Münster TPC was indeed improved over separate light and charge calibrations. An elaboration of the saturation effects that were observed in the ^{137}Cs measurement and the options to approach these effects is needed. For example, a saturation correction via the PAX data processor could be set up for this purpose. Eventually, the NEST model for scintillation and ionization processes in liquid xenon was used to calculate the light and charge yield for a range of energies.

An energy calibration with more sources, for example 122 kev photons from ^{57}Co,

α emitters, and neutron sources to measure nuclear recoils, would refine the results of this work. Multiple calibration sources should be measured simultaneously in a single data taking process to bypass liquid level instabilities and their effect on the charge yield. Nevertheless, a measurement of the liquid level stability of the TPC, independent of the capacitive level meters, should be integrated to support the level meters. Monitoring the charge over light yield ratio over time with a specific calibration source, e.g. ^{83m}Kr, would serve this purpose.

The detector system was originally intended as a test station for XENON100 and XENON1T, for example as a purity monitor via measuring the electron lifetime. This work provides the knowledge and many techniques that are necessary for a further development of this project.

A Appendix

Current Gas System Setup

The gas system is used for various purposes and is under constant change. The setup throughout the process of this work is shown here in detail.

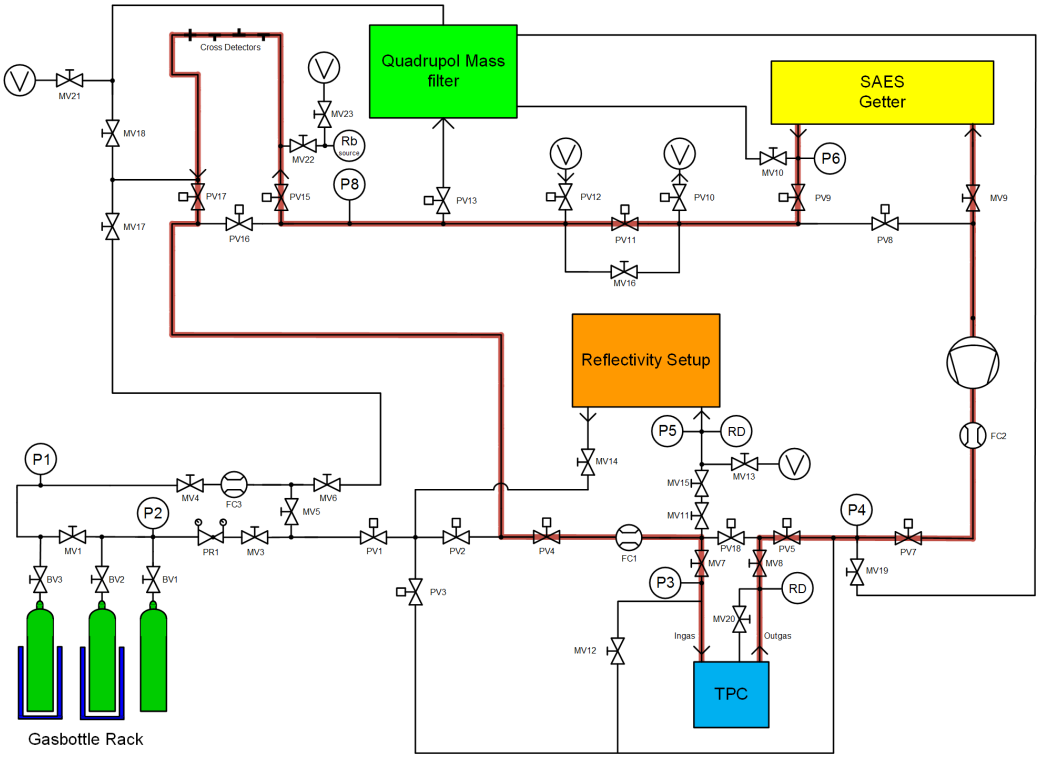

Figure A.1 – Updated version of the gas system hosting the Münster TPC. The xenon path during operation in the ^{83m}Kr data acquisition is highlighted. The ^{83}Rb valve was closed during the background and ^{137}Cs measurements.

S1 and S2 Spectra of the ^{83m}Kr and ^{137}Cs Energy Lines

The corrected S1 and S2 spectra for each calibration line are shown in figure A.2 and A.3. They are used in section 5.3 to show the improvement in resolution when both readout channels are combined.

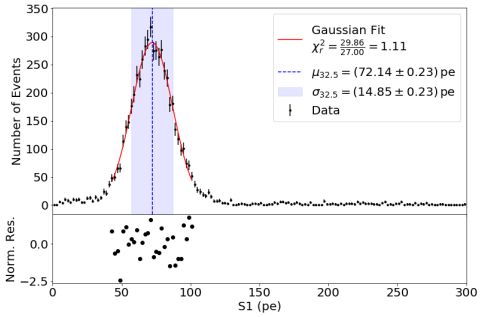

(a) S1 spectrum of 32.1 keV signature.

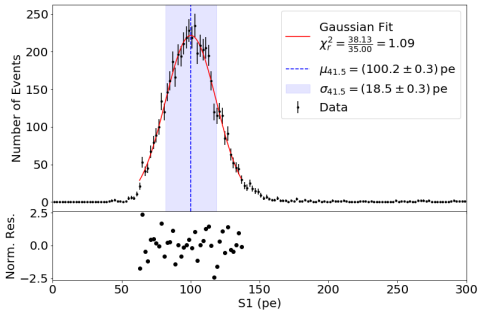

(b) S1 spectrum of 41.5 keV signature.

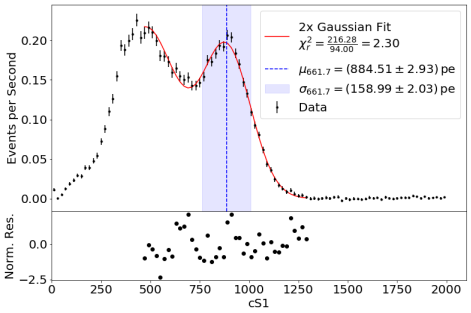

(c) S1 spectrum of 661.7 keV signature.

Figure A.2 – S1 spectra of the calibration sources. The former two are fitted via Gaussian functions, the latter via the sum of two Gaussian functions.

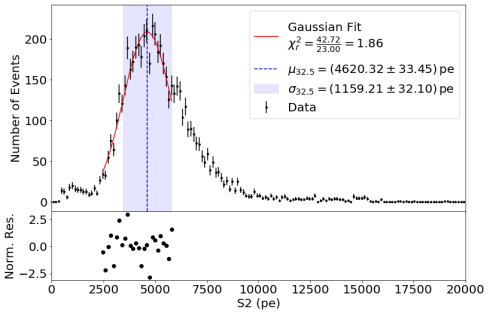

(a) S2 spectrum of 32.1 keV signature.

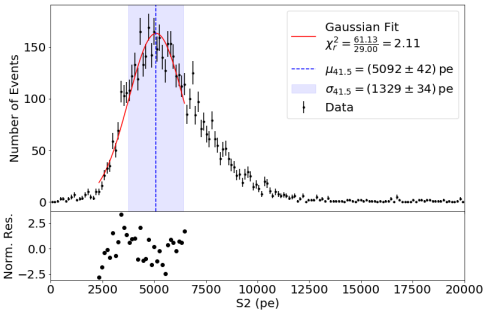

(b) S2 spectrum of 41.5 keV signature.

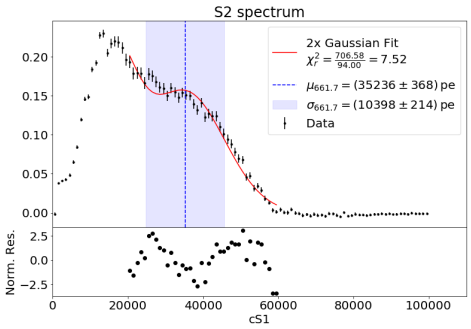

(c) S2 spectrum of 661.7 keV signature.

Figure A.3 – S2 spectra of the calibration sources. The former two are fitted via Gaussian functions, the latter via the sum of two Gaussian functions.

Bibliography

[1] J. B. Albert et al. Improved measurement of the $2\nu\beta\beta$ half-life of ^{136}xe with the exo-200 detector. *Phys. Rev.*, C89(1):015502, 2014.

[2] J. B. Albert et al. Search for majorana neutrinos with the first two years of exo-200 data. *Nature*, 510:229–234, 2014.

[3] L. Althüser. Geant4 simulations of the muenster dual phase xenon tpc. Bachelors thesis, Institut für Kernphysik, Westfälische Wilhelms-Universität Münster, 2015.

[4] E. Aprile and T. Doke. Liquid xenon detectors for particle physics and astrophysics. *Reviews of Modern Physics*, 82(3):2053, 2010.

[5] E. Aprile et al. Simultaneous measurement of ionization and scintillation from nuclear recoils in liquid xenon for a dark matter experiment. *Phys. Rev. Lett.*, 97:081302, Aug 2006.

[6] E. Aprile et al. Observation of anticorrelation between scintillation and ionization for mev gamma rays in liquid xenon. *Phys. Rev. B*, 76:014115, Jul 2007.

[7] E. Aprile et al. First dark matter results from the xenon100 experiment. *Physical Review Letters*, 105(13):131302, 2010.

[8] E. Aprile et al. The xenon100 dark matter experiment. *Astroparticle Physics*, 35(9):573–590, 2012.

[9] E. Aprile et al. Analysis of the xenon100 dark matter search data. *Astroparticle Physics*, 54:11–24, 2014.

[10] E. Aprile et al. Observation and applications of single-electron charge signals in the xenon100 experiment. *J. Phys.*, G41:035201, 2014.

[11] E. Aprile et al. First dark matter search results from the xenon1t experiment. *Physical review letters*, 119(18):181301, 2017.

[12] E. Aprile et al. Online ^{222}rn removal by cryogenic distillation in the xenon100 experiment. *The European Physical Journal C*, 77(6):358, May 2017.

[13] E. Aprile et al. Dark matter search results from a one tonne × year exposure of xenon1t. *arXiv preprint arXiv:1805.12562*, 2018.

[14] G. Bakale, U. Sowada, and W. F. Schmidt. Effect of an electric field on electron attachment to sulfur hexafluoride, nitrous oxide, and molecular oxygen in liquid argon and xenon. *The Journal of Physical Chemistry*, 80(23):2556–2559, 1976.

[15] M. J. Berger et al. Xcom: Photon cross sections database (version 1.5). *National Institute of Standards and Technology, Gaithersburg, MD*, 2010.

[16] A. Bolozdynya. Chapter 18 - noble gas detectors. In M. N. Wernick and J. N. Aarsvold, editors, *Emission Tomography*, pages 359 – 381. Academic Press, San Diego, 2004.

[17] E. Browne and J. K. Tuli. Nudat 2.0: Nuclear structure and decay data on the internet. *Nuclear Data Sheets 108,2173*, 2007.

[18] A. Buss. Characterization of the mÜnster dual phase xenon tpc and of a newly developed magnetically driven piston pump. Masters thesis, Institut für Kernphysik, Westfälische Wilhelms-Universität Münster, 2016.

[19] CAEN. *User Manual UM3248 V1724/VX1724 8 Channels 14bit 100 MS/s Digitizer*. CAEN, 32 edition, April 2017.

[20] T. Doke et al. Estimation of fano factors in liquid argon, krypton, xenon and xenon-doped liquid argon. *Nuclear Instruments and Methods*, 134(2):353–357, 1976.

[21] T. Doke et al. Absolute scintillation yields in liquid argon and xenon for various particles. *Japanese journal of applied physics*, 41(3R):1538, 2002.

[22] K. Giboni et al. Compton positron emission tomography with a liquid xenon time projection chamber. *Journal of Instrumentation*, 2(10):P10001, 2007.

[23] J. Jortner et al. Localized excitations in condensed ne, ar, kr, and xe. *The Journal of chemical physics*, 42(12):4250–4253, 1965.

[24] R. K. Kirby. Thermal expansion of polytetrafluoroethylene (teflon) from −190 °c to +300 °c. *Journal of Research of the National Bureau of Standards*, 57(2):91–94, 1956.

[25] A. Kish. *Dark matter search with the XENON100 experiment.* PhD thesis, Universität Zürich, 2011.

[26] G. F. Knoll. *Radiation detection and measurement.* John Wiley & Sons, 2010.

[27] C. Levy. *Light Propagation and Reflection off Teflon in Liquid Xenon Detectors for the XENON100 and XENON1T Dark Matter Experiment.* PhD thesis, Institut für Kernphysik, Westfälische Wilhelms-Universität Münster, 2014.

[28] E. A. McCutchan. Nudat 2.0: Nuclear structure and decay data on the internet. *Nuclear Data Sheets 125, 201*, 2015.

[29] L. S. Miller, S. Howe, and W. E. Spear. Charge transport in solid and liquid ar, kr, and xe. *Phys. Rev.*, 166:871–878, Feb 1968.

[30] K. Ni. *Development of a liquid xenon time projection chamber for the XENON dark matter Search.* PhD thesis, Columbia University, 2006.

[31] K. Ozone. *Liquid Xenon Scintillation Detector for the New Search Experiment.* PhD thesis, University of Tokyo, 2005.

[32] S. Rosendahl. *Gas purification of the XENON dark matter search.* PhD thesis, Institut für Kernphysik, Westfälische Wilhelms-Universität Münster, 2015.

[33] D. Schulte. Capacitance-based levelmeter read-out for the münster dual phase xenon time projection chamber. Bachelors thesis, Institut für Kernphysik, Westfälische Wilhelms-Universität Münster, 2016.

[34] J. Schulz. Design of a 2-phase xenon time projection chamber for electron drift length measurements. Diploma thesis, Institut für Kernphysik, Westfälische Wilhelms-Universität Münster, 2011.

[35] H. Schulze Eissing. Investigations of the münster dual phase xenon time projection chamber. Bachelors thesis, Institut für Kernphysik, Westfälische Wilhelms-Universität Münster, 2017.

[36] P. Sorensen. Anisotropic diffusion of electrons in liquid xenon with application to improving the sensitivity of direct dark matter searches. *Nuclear Instruments and Methods in Physics Research Section A: Accelerators, Spectrometers, Detectors and Associated Equipment*, 635(1):41–43, 2011.

[37] M. Szydagis et al. Nest: a comprehensive model for scintillation yield in liquid xenon. *Journal of Instrumentation*, 6(10):P10002, 2011.

[38] M. Szydagis et al. Enhancement of nest capabilities for simulating low-energy recoils in liquid xenon. *Journal of Instrumentation*, 8(10):C10003, 2013.

[39] T. Takahashi et al. Average energy expended per ion pair in liquid xenon. *Physical Review A*, 12(5):1771, 1975.

[40] M. Tanaka et al. Let dependence of scintillation yields in liquid xenon. *Nuclear Instruments and Methods in Physics Research Section A: Accelerators, Spectrometers, Detectors and Associated Equipment*, 457(3):454–463, 2001.

[41] C. Wittweg. Xenon100 dark matter search with the pax raw data processor for xenon1t. Masters thesis, Institut für Kernphysik, Westfälische Wilhelms-Universität Münster, 2016.

Danksagung

An dieser Stelle möchte ich in riesengroßes, vielfältiges Dankeschön aussprechen!

Ein großer Dank geht an Herrn Prof. Dr. C. Weinheimer für die Möglichkeit, an einer komplexen Apparatur zu arbeiten und von Laborarbeit bis Datenanalyse sämtliche Höhen und Tiefen zu erleben. Die oft bloß kleinen, aber entscheidenden Tipps erlaubten meist signifikante Fortschritte. Vielen Dank auch für die Förderung der Teilnahme an einer DPG Tagung und der Astroteilchenschule Obertrubach, das waren wertvolle Erfahrungen!

Herrn Prof. Dr. A. Kappes danke ich für die Übernahme der Zweitkorrektur meiner Arbeit.

Christian Wittweg, vielen Dank für die vielen Hilfestellungen, die du mir mit beachtenswerter Geduld und Klarheit gegeben hast. Es sagt dir zwar keiner, aber deine Witze sind spitze, weiter so! Ach, und deine Korrekturen sind wirklich so hilfreich wie behauptet wird!
Michael Murra, durch dich habe ich das komplexe System im Labor inzwischen ganz gut verstanden. Dein Einsatz, stellenweise spät abends und am Wochenende, hat ganz entscheidend zu einem Gelingen meiner Arbeit beigetragen.
Alex Fieguth, vielen Dank, für die Einführung in die Arbeitsgruppe. Wenn ich mal nicht weiterkam, waren deine Hinweise Gold wert!
Für die Anmerkungen zu meiner Arbeit bedanke ich mich herzlich bei Lutz Althüser und Miguel Vargas. Durch euch hat meine Arbeit eindeutig an Lesbarkeit gewonnen.
Danke an die gesamte XENON-Gruppe für die herzliche Aufnahme, Rat und Tat in allen Fragen und eine spannende, lehrreiche und gute Zeit. Ich habe – dank euch – sehr, sehr viel gelernt!

Einen herzlichen Dank möchte ich meinen Eltern, Anke und Rainer Gauda, aussprechen. Nur durch eure Unterstützung und Geduld wurde mir ein erfolgreiches Studium ermöglicht.

Niklas, dir gilt hier noch eine besondere Erwähnung. Dieses Studium hat uns viel abverlangt, doch zusammen haben wir es irgendwie überlebt. Danke für die Studienzeit meines Lebens!

Ruth, Danke, dass du immer für mich da warst und bist!